AIAA JOURNAL
Vol. 49, No. 11, November 2011

Stochastic Method for Airfoil Self-Noise Computation in Frequency Domain

Damiano Casalino* and Mattia Barbarino†
Centro Italiano Ricerche Aerospaziali, I-81043 Capua, Italy

DOI: 10.2514/1.J050773

A stochastic Fourier method for the computation of synthetic solenoidal velocity fluctuations from a steady Reynolds-averaged Navier–Stokes solution is revised, validated against jet-noise experimental data, and applied to the problem of noise radiation from the trailing edge of a NACA-0012 airfoil. The method is used to compute the source term of the Howe's acoustic analogy equation for an isentropic flow that is solved in the frequency domain using a finite element discretization. For each spectral component of the source term, a prescribed number of realizations of the synthetic source field is generated by seeding the random number generator. The corresponding sound fields are then computed and finally averaged to track statistically converged noise spectra. The self-noise spectra computed for an airfoil at different values of the freestream velocity are compared with literature experimental data and semianalytical predictions. It is shown that the finite element results are in fairly good agreement with both the semianalytical results and the measurements.

Nomenclature

B'	=	acoustic stagnation enthalpy
$\mathcal{C}$	=	spanwise correlation parameter
c_0	=	speed of sound
$c_{1,\ldots,4}$	=	stochastic model parameters
D	=	nozzle diameter
E	=	monodimensional turbulent kinetic energy spectrum
i	=	imaginary unit; $(\sqrt{-1})$
K	=	turbulent kinetic energy
$\mathcal{K}$	=	filter function
k	=	acoustic wave number ($k = \omega/c_a$)
$\mathbf{k}$	=	turbulent wave vector
k_e	=	wave number of maximum E
k_η	=	Kolmogorov wave number
L	=	span length
$\tilde{l}$	=	average correlation length
L_p	=	noise power level
L_T	=	turbulence integral length scale
$\mathbf{n}$	=	normal unit vector
N_F	=	number of Fourier modes
N_w	=	number of grid points per Fourier component
$\mathcal{P}$	=	probability density function
p'	=	acoustic pressure
R	=	microphone radial distance
$\hat{r}$, $\hat{R}$	=	generic random and filtered random quantities
Re_c	=	airfoil Reynolds number based on chord
Re_D	=	jet Reynolds number based on nozzle diameter
T'_{ij}	=	Lighthill's stress tensor in the convected reference frame
U_e	=	asymptotic boundary-layer velocity
U_j, M_j	=	jet centerline velocity and Mach number at nozzle
$\hat{u}_n$, ψ_n, $\boldsymbol{\sigma}_n$	=	magnitude, phase, and direction of nth Fourier component of $\mathbf{u}'$
$\mathbf{u}'$, $\boldsymbol{\omega}'$	=	fluctuating (turbulent) velocity and vorticity
W_0, $\mathbf{W}_1$	=	finite element method test functions
y^+	=	dimensionless distance from wall; $y\sqrt{\tau_w/\rho_0}/\nu$
α, ϕ, θ	=	turbulent wave vector random angles
δ	=	Dirac function
ϵ	=	turbulent dissipation rate
ν	=	kinematical viscosity
ρ	=	correlation coefficient
ρ_0, T_0, p_0, $\mathbf{U}$	=	mean-flow density, temperature, pressure, and velocity
ϱ	=	vortex convection velocity ratio
$\boldsymbol{\tau}$	=	tangential unit vector
τ_{ij}	=	viscous stress tensor
τ_w	=	wall shear stress
ϕ'	=	acoustic velocity potential
ω	=	radian frequency or specific turbulent dissipation rate

Subscripts

a	=	atmospheric ambient or freestream conditions
n	=	surface normal vector component or nth Fourier component
τ	=	surface tangential vector component

Superscript

~	=	dimensionless mean-flow quantities

I. Introduction

THE development of stochastic computational aeroacoustics (CAA) approaches for the prediction of broadband noise spectra from wall-bounded turbulent flows has received a great deal of interest in recent years, in particular, in the domain of wing high-lift device noise [1,2]. The main focus is on the development of methods that can be used for multiobjective optimizations of wing profiles in conjunction with two-dimensional (2-D) steady Reynolds-averaged Navier–Stokes (RANS) computations and for the final three-dimensional (3-D) assessment of a wing low-noise design.

Two families of methods are currently used for the generation of synthetic turbulence. The first one was introduced by Kraichnan [3], and it is based on the idea that Fourier components of solenoidal velocity fluctuations can be sampled in the wave-number space from a prescribed monodimensional energy spectrum. An extension of the Fourier approach to simulate the different kinematics and statistics of

Presented as Paper 2010-3884 at the 16th AIAA/CEAS Aeroacoustics Conference, Stockholm, 7–9 June 2010; received 23 July 2010; revision received 26 May 2011; accepted for publication 13 June 2011.

*Research Engineer, Aerodynamics and Aeroacoustics laboratory. Member AIAA.

†Research Engineer, Aerodynamics and Aeroacoustics Laboratory.

large- and small-scale eddies was proposed by Fung et al. [4]. The second family of stochastic methods is based on the idea put forward by Careta et al. [5], according to which turbulent fluctuations of prescribed two-point statistical properties can be obtained by filtering white noise. The revision and improvement of these methods for aeroacoustic applications have produced the stochastic noise generation and radiation (SNGR) method on one side [6–8] and the random particle mesh (RPM) method on the other side [9–11].

The advantages of the SNGR method are its simplicity and the possibility to control the spectral content of the velocity fluctuations, whereas the main advantage of the RPM method lies in the possibility to control the two-point space correlation by defining suitable digital filters. A recognized drawback of the SNGR method is the computational time and memory occupation, due to the large amount of information to be produces and managed at each grid point. But the computational time is an issue also for the RPM method, since it requires the projection of flow data from the computational fluid dynamics (CFD) mesh to the CAA mesh every time step. The SNGR method has been revised in this paper in order to relax its two limitations. In particular, the reduction of computational time and memory occupation has been achieved through a careful architectural conception of the code for which the description, however, is not in the scope of the present work; the control of the two-point correlation of the velocity fluctuations has been improved with respect to the standard SNGR model by using a blob-texture generation algorithm, based on the local value of the turbulence correlation length, and by applying a digital filter to the stochastic variables of the model.

To validate the present stochastic model and to investigate its sensitivity to some model parameters, the noise from a round jet of Reynolds number 5.8×10^5 and Mach number 0.585 has been predicted and compared with anechoic wind-tunnel measurements, originally reported in this work. The noise prediction has been carried out by convoluting the vortex-sound source terms with the free-space Green's function in the hypothesis of negligible mean-flow convection effects. Thus, Powell's acoustic analogy model [12] has been used. Following the analysis of Crow [13], in fact, the Powell's equation [12] is equivalent to the Lighthill's equation [14] in the case of a low Mach number flow. The same theoretical arguments have been used in this work to show that, in the case of a convected acoustic analogy model, the vortex-sound source term that is compatible with a convected Lighthill's equation is the nonlinear Lamb vector $\mathcal{L}'' = \boldsymbol{\omega}' \times \mathbf{u}'$.

A further validation of the stochastic model has been successively conducted by computing the trailing-edge noise from a NACA-0012 airfoil and comparing the numerical results with the experimental data by Brooks et al. [15]. A 2-D/3-D correction procedure has been applied to recover the 3-D noise levels from 2-D acoustic computations, as suggested by Ewert et al. [2]. Furthermore, a semianalytical method based on the classical model by Amiet [16] has been used to produce further reference data for the validation of the stochastic method. One of the original aspects of this work is that the synthetic velocity fluctuations are used to compute the source terms of the Howe's acoustic analogy equation [17], which is solved in the frequency domain using a finite element method (FEM). The velocity signals are used to compute the components of the turbulent Lamb vector in each cell of the CFD mesh. The Fourier components of the Lamb vector are exported as a discrete distribution of dipoles that are projected on the CAA mesh and then integrated as Dirac dipoles by taking advantage of the weak formulation. Moreover, a number of different realizations of the synthetic source field are generated by seeding the random number generator. For each source realization, the noise spectra are computed and finally averaged to achieve statistically converged results. The frequency-domain FEM computation is carried out by making a massive use of the restart capabilities of the CAA code *Opty∂B*. As a consequence, after the first frequency run, the solution of the linear system and the solution interpolation at prescribed microphone locations are the only computational operations undertaken by the code. The open-source direct linear system solver MUMPS [18] is used, for which the multi-right-hand-side capabilities allow us to efficiently manage the different source realizations.

The main goal of this paper is to make an assessment of the improved SNGR method in view of the airframe-noise analyses to be carried out in the framework of the Clean Sky: Green Regional Aircraft project funded by the European Commission. The method has been recently implemented in the code *Opty∂B*-SNGR, which has been designed in order to enable an automatic partition of the stochastic generation and thus reduce the amount of allocated memory. Furthermore, the CPU time has been significantly reduced by exploiting trivial rules of software optimization for operations involving trigonometric, logarithmic, and exponential functions. Notice that part of this work has been presented as a conference paper in [19], the main differences being the inclusion of the jet-noise validation, the computation of the NACA-0012 trailing-edge noise from fully transitioned RANS solutions, and the use of a different wall pressure spectrum model in the semianalytical noise prediction.

The remainder of this paper is organized as follows. The noise propagation model and the stochastic noise source model are described in Secs. II and III, respectively. The jet-noise numerical results and their comparison with the experimental data are presented in Sec. IV. The NACA-0012 RANS solutions are described in Sec. V and validated against experimental data from [15]. The acoustic results are then presented in Sec. VI and compared with both experimental data [15] and semianalytical predictions. Conclusive remarks are finally made in Sec. VII.

II. Noise Propagation Model

This section describes the wave model used in the present study. It is based on the vortex-sound acoustic analogy model in the form derived by Howe [17]. Considering a compressible inviscid perfect homentropic gas mean flow, and by rearranging the continuity equation and the linear momentum equation in the form of Crocco's equation, an acoustic analogy equation for the stagnation enthalpy B can be obtained for which the linearized form is

$$\frac{1}{\rho_0}\nabla\cdot(\rho_0\nabla B') - \frac{D_0}{Dt}\left(\frac{1}{c_0^2}\frac{D_0 B'}{Dt}\right) = \frac{1}{\rho_0}\nabla\cdot(\rho_0\boldsymbol{\omega}'\times\mathbf{u}') \qquad (1)$$

where $D_0/Dt = \partial/\partial t + \mathbf{U}\cdot\nabla$ is the linearized Lagrangian derivative, with the subscripts of 0 denoting time-averaged quantities and primes denoting fluctuations. Throughout, unless otherwise stated, vectors are denoted with bold symbols. In the linear propagation field, the stagnation enthalpy fluctuation is related to the acoustic pressure by the following relationship:

$$\frac{D_0 B'}{Dt} = \frac{1}{\rho_0}\frac{\partial p'}{\partial t} \qquad (2)$$

The source term at the right-hand side of Eq. (1) has been obtained under two assumptions. The first one is that, for the scope of the present work, the unsteady flow fluctuations induced by the vortical flow motion are the main sources of aerodynamic noise and the entropic fluctuations can be neglected. The second assumption is that only the nonlinear component of the Lamb vector is compatible with a convected acoustic analogy model. To justify this assumption, it is useful to derive the Lighthill acoustic analogy equation in a uniformly convected flow. The continuity and linear momentum equations can be written in the following forms:

$$\frac{D_0\rho}{Dt} = -\frac{\partial(\rho u_i)}{\partial x_i} + U_i\frac{\partial\rho}{\partial x_i} = -\frac{\partial(\rho u_i')}{\partial x_i} \qquad (3)$$

$$\frac{D_0}{Dt}(\rho u_i') = -\frac{\partial p}{\partial x_i} + \frac{\partial\tau_{ij}}{\partial x_j} = -\frac{\partial(\rho u_i' u_j')}{\partial x_j} \qquad (4)$$

where use of the Einstein index summation convention has been made for practical convenience. Then, by introducing the relative Lighthill stress tensor

$$T'_{ij} = \rho u'_i u'_j + [p - c_0^2(\rho - \rho_0)]\delta_{ij} - \tau_{ij}$$

Equation (4) takes the following form:

$$\frac{D_0}{Dt}(\rho u'_i) + c_0^2 \frac{\partial(\rho - \rho_0)}{\partial x_i} = -\frac{\partial T'_{ij}}{\partial x_j} \tag{5}$$

Finally, using D_0 [Eq. (3)]/$Dt - \partial$ [Eq. (5)]/∂x_i leads to the convected Lighthill equation:

$$\left(\frac{1}{c_0^2}\frac{D_0^2}{Dt^2} - \frac{\partial^2}{\partial x^2}\right)[(\rho - \rho_0)c_0^2] = \frac{\partial^2 T'_{ij}}{\partial x_i \partial x_j} \tag{6}$$

By supposing that the perturbation velocity field is solenoidal and the entropic fluctuations are negligible (low Mach number flow), by neglecting the viscous stress contribution, and coming back to the vectorial notation, the convected Lighthill wave equation takes the following approximated form:

$$\left(\frac{1}{c_0^2}\frac{D_0^2}{Dt^2} - \nabla^2\right)p' \simeq \rho_0 \nabla \cdot (\boldsymbol{\omega}' \times \mathbf{u}') + \rho_0 \nabla^2\left(\frac{u'^2}{2}\right) \tag{7}$$

Following the dimensional analysis made by Crow [13] on sound generated by a compact turbulent eddy, it can be demonstrated that the noise generated by the second source term is negligible when the characteristic eddy fluctuation Mach number u'/c_0 is small. It is possible to achieve the same conclusion by considering the frequency counterpart of Eq. (7) and convoluting it with the convected Green's function. Hence, integrating by parts one time for the first term and twice for the second term, the far-field acoustic pressures generated by the second and first terms result in the ratio $k^2{:}k/L_T = kL_T$, where k is the acoustic wave number and L_T is the integral scale of the turbulent eddy. Assuming that the characteristic frequency of a turbulent eddy scales as u'/L_T, then the reduced frequency kL_T scales as u'/c_0. Hence, the noise power level ratio scales as the square of the perturbation Mach number. From this analysis, it follows that the source term at the right-hand side of the linearized Howe Eq. (1) that is compatible with the Lighthill acoustic analogy model is the nonlinear Lamb vector $\mathcal{L}'' = \boldsymbol{\omega}' \times \mathbf{u}'$.

The frequency-domain counterparts of Eqs. (1) and (2), under the $-i\omega t$ convention, are

$$\begin{aligned} &k^2\frac{B'}{\tilde{T}} + k\left(\frac{2i}{\tilde{T}}\tilde{U}\cdot\nabla B' - \frac{i\tilde{U}\cdot\nabla\tilde{T}}{\tilde{T}^2}B'\right) + \frac{\nabla\tilde{\rho}}{\tilde{\rho}}\cdot\nabla B' + \nabla^2 B' \\ &\quad - \nabla\cdot\left(\frac{\tilde{U}}{\tilde{T}}\tilde{U}\cdot\nabla B'\right) + \frac{\nabla\cdot\tilde{U}}{\tilde{T}}\tilde{U}\cdot\nabla B' = -\frac{1}{\tilde{\rho}}\nabla\cdot(\tilde{\rho}\,\widehat{\boldsymbol{\omega}'\times\mathbf{u}'}) \\ &\quad p' = \tilde{\rho}\rho_a\left(B' + \frac{i}{k}\tilde{U}\cdot\nabla B'\right) \end{aligned} \tag{8}$$

where dimensionless mean-flow quantities have been denoted by $\tilde{\cdot}$ and are referred to the ambient speed of sound c_a, density ρ_a, and temperature T_a. The hat symbol upon $\boldsymbol{\omega}' \times \mathbf{u}'$ at the right-hand side denotes Fourier transform of the Lamb vector. The wave equation has been factorized in the acoustic wave number $k = \omega/c_a$.

The propagation kernel of Eq. (1) is the same as the one obtained by Pierce [20] for acoustic potential fluctuations ϕ' superimposed to a rotational mean flow under the assumption of slowly varying mean flow over the length and time scales of the sound waves (high-frequency limit). Since out of the source region the flow is typically irrotational, it results from Crocco's equation that $B' = ikc_a\phi'$. Therefore, it immediately follows that the Howe and Pierce equations lead to the same acoustic pressure solution out of the source region in the presence of a uniform flow, provided that consistent source terms are specified.

A weak form of Eq. (8) can be now obtained by weighting the equation against the test function W_0 over the whole computational domain; that is,

$$\begin{aligned} &\int_V W_0\left[k^2\frac{B'}{\tilde{T}} + k\left(\frac{2i}{\tilde{T}}\tilde{\mathbf{U}}\cdot\nabla B' - \frac{i\tilde{\mathbf{U}}\cdot\nabla\tilde{T}}{\tilde{T}^2}B'\right) + \frac{\nabla\tilde{\rho}}{\tilde{\rho}}\cdot\nabla B'\right. \\ &\qquad \left. + \nabla\cdot\left(\nabla B' - \frac{\tilde{\mathbf{U}}}{\tilde{T}}\tilde{\mathbf{U}}\cdot\nabla B'\right) + \frac{\nabla\cdot\tilde{\mathbf{U}}}{\tilde{T}}\tilde{\mathbf{U}}\cdot\nabla B'\right]\mathrm{d}v \\ &\quad = -\int_V \frac{W_0}{\tilde{\rho}}\nabla\cdot(\tilde{\rho}\,\widehat{\boldsymbol{\omega}'\times\mathbf{u}'})\,\mathrm{d}v \end{aligned} \tag{9}$$

Then, by integrating by parts, making use of the Gauss theorem, and introducing the gradient test function $\mathbf{W}_1 = \nabla W_0$, the following weak-form follows:

$$\begin{aligned} &\int_V\left[k^2 W_0\frac{B'}{\tilde{T}} + kW_0\left(\frac{2i}{\tilde{T}}\tilde{\mathbf{U}}\cdot\nabla B' - \frac{i\tilde{\mathbf{U}}\cdot\nabla\tilde{T}}{\tilde{T}^2}B'\right) + W_0\frac{\nabla\tilde{\rho}}{\tilde{\rho}}\cdot\nabla B'\right. \\ &\qquad \left. - \left(\nabla B' - \frac{\tilde{\mathbf{U}}}{\tilde{T}}\tilde{\mathbf{U}}\cdot\nabla B'\right)\cdot\mathbf{W}_1 + W_0\frac{\nabla\cdot\tilde{\mathbf{U}}}{\tilde{T}}\tilde{\mathbf{U}}\cdot\nabla B'\right]\mathrm{d}v \\ &\qquad - \int_S W_0\frac{\partial B'}{\partial n}\left(1 - \frac{\tilde{U}_n^2}{\tilde{T}}\right)\mathrm{d}s + \int_S W_0\frac{\partial B'}{\partial\tau}\frac{\tilde{U}_n\tilde{U}_\tau}{\tilde{T}}\,\mathrm{d}s \\ &\quad = \int_V(\widehat{\boldsymbol{\omega}'\times\mathbf{u}'})\cdot\left(\mathbf{W}_1 - \frac{W_0}{\tilde{\rho}}\nabla\tilde{\rho}\right)\mathrm{d}v \end{aligned} \tag{10}$$

with

$$\begin{aligned} &\tilde{\mathbf{U}} = \tilde{U}_n\mathbf{n} + (\tilde{\mathbf{U}} - \tilde{U}_n\mathbf{n}) \equiv \tilde{U}_n\mathbf{n} + \tilde{U}_\tau\boldsymbol{\tau} \\ &\text{where } \boldsymbol{\tau} = (\tilde{\mathbf{U}} - \tilde{U}_n\mathbf{n})/\tilde{U}_\tau \quad \text{and} \quad \tilde{U}_\tau = |\tilde{\mathbf{U}} - \tilde{U}_n\mathbf{n}| \end{aligned} \tag{11}$$

The normal derivative of B' in the first surface integral accounts for the boundary conditions of the problem. By supposing that the flow is irrotational at the boundaries of the computational domain ($B' = ikc_a\phi'$), the same boundary condition used for the Pierce wave equation can be applied. In particular, for hard solid surfaces, a vanishing normal derivative of B' can be imposed.

Nonreflecting radiation conditions are prescribed through a perfectly matched layer (PML) approach, consisting of applying the following change of variables to the shape functions of the first-order derivatives and to the corresponding first-order test functions: $\partial/\partial x_i \to \alpha(x_i)\partial/\partial x_i$, with $\alpha(x_i) = 1/(1 + i\sigma_i)$ and σ_i denoting the PML damping factor along the x_i direction. To ensure a smoother transition from the physical domain to the PML buffers, the damping factor σ is increased from zero to a maximum value at the external boundary with a quadratic law. The volume integration is then transformed consistently using

$$\mathrm{d}v \to \prod_i (1 + i\sigma_i)\,\mathrm{d}v$$

One of the advantages of a weak-form discretization is the capability to deal with Dirac source distributions directly, thus avoiding the numerical desingularization of the source by using, for instance, an equivalent Gaussian function to reproduce the effect of a Dirac source in a very small volume around the source. This property is very useful to solve an acoustic analogy equation with source terms computed from a CFD solution. Terms of the form

$$\int_V f W_0\,\mathrm{d}V$$

and

$$\int_V \mathbf{f}\cdot\mathbf{W_1}\,\mathrm{d}V$$

are present at the right-hand side of Eq. (10), where f and $\mathbf{f}$ denote generic scalar and vectorial functions of the flow fluctuations, respectively. A convenient way to compute these source integrals consists of integrating the source functions (cell by cell) on the CFD mesh and then projecting the integrated values on the CAA mesh as a set of Dirac sources. Integrals involving Diracs, i.e.,

$$\int_V \delta(\mathbf{x}-\mathbf{x}_s)W_0(\mathbf{x})\,\mathrm{d}V$$

and Dirac dipoles, i.e.,

$$\int_V \delta(\mathbf{x}-\mathbf{x}_s)\boldsymbol{\tau}_s\cdot\mathbf{W}_1(\mathbf{x})\,\mathrm{d}V$$

are finally computed on the CAA mesh and used to construct the right-hand side of the wave equation. To better explain the source projection algorithm from the CFD to the CAA mesh, it is useful to consider the dipole source term at the right-hand side of Eq. (10) and suppose that the Lamb vector component is computed at the centroid of each CFD cell (subscript s). The following numerical integration rule is applied:

$$\int_V \widehat{\boldsymbol{\omega}'\times\mathbf{u}'}\cdot\mathbf{W}_1\,\mathrm{d}V \simeq \sum_{j=1}^{J}\int_{V_j}\sum_{k=1}^{K^j} V_k\delta(\mathbf{x}-\mathbf{x}_s)\widehat{\boldsymbol{\omega}'_s\times\mathbf{u}'_s}\cdot\mathbf{W}_1(\mathbf{x})\,\mathrm{d}V$$

$$=\sum_{j=1}^{J}\sum_{k=1}^{K^j} V_k\widehat{\boldsymbol{\omega}'_s\times\mathbf{u}'_s}\cdot\mathbf{W}_1^j(\mathbf{x}_s) \tag{12}$$

where J is the number of CAA cells, K^j is the number of CFD cells for which the centroid falls inside the CAA cell j, V_k is the volume of the CFD cell k, and $\mathbf{W}^j$ are the first-derivative FEM shape functions in the CAA cell j.

Details about the verification and validation of the $Opty\partial B$ sound propagation capabilities are reported in [21].

III. Noise Generation Model

This section describes the method used to synthesize a Lamb vector field $\mathcal{L}'' = \boldsymbol{\omega}'\times\mathbf{u}'$ from a steady RANS solution, to be used as a source term in Eq. (10). A revised SNGR method has been employed, as resulting from a validation process undertaken for both jet- and airframe-noise problems. Many sophistications of the method have been tested during this process that finally led to a reasonably simple formulation. All the details are provided hereafter as a guarantee of repeatability of the numerical results described in Secs. IV and VI.

Following the concept put forward by Kraichnan [3], turbulent velocity fluctuation can be computed as a sum of Fourier components; that is,

$$\mathbf{u}'(\mathbf{x},t)=2\sum_{n=1}^{N_F}\hat{u}_n\cos\{\mathbf{k}_n\cdot(\mathbf{x}-\varrho\mathbf{U}t)+\psi_n\}\boldsymbol{\sigma}_n \tag{13}$$

where $\hat{u}_n$, ψ_n, and $\boldsymbol{\sigma}_n$ are the magnitude, phase, and direction of the nth Fourier component, respectively. As proposed by Bailly and Juvé [7], each Fourier mode is supposed to be convected at the local mean-flow velocity $\mathbf{U}$, corrected by the vortex convection velocity ratio ϱ. This factor may account for the wall induction effect that reduces the vortex convection velocity with respect to the mean-flow velocity at the location of the vortex core. For the airfoil self-noise prediction of Sec. VI, the value $\varrho=0.9$ has been used. The factor may also account for the vortical induction in a jet shear layer, but this effect is negligible for low-speed subsonic jets. For the jet-noise prediction of Sec. IV, the value $\varrho=1$ has been therefore assumed. Notice that the scalar product $\varrho\mathbf{k}_n\cdot\mathbf{U}$ in Eq. (13) accounts for the local time variation of the velocity field. Assuming incompressibility, the zero divergence condition applied to Eq. (13) results in the relationship $\mathbf{k}_n\cdot\boldsymbol{\sigma}_n=0$, stating that the wave vector is perpendicular to the velocity vector.

By supposing that the turbulent flowfield is isotropic, the magnitude of the nth Fourier mode is related to the monodimensional energy spectrum $E(k)$ by the expression $\hat{u}_n=\sqrt{E(k_n)\Delta k_n}$, where k_n and Δk_n are the wave number and the corresponding band of the nth mode. The von Kármán–Pao isotropic turbulence spectrum has been used; that is,

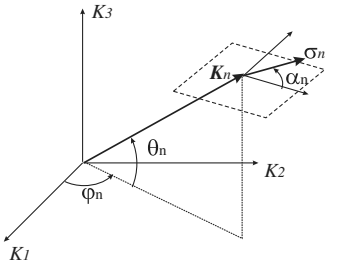

Fig. 1 Representation of the wave vector k_n and velocity direction vector σ_n, and definition of the stochastic angles.

$$E(k)=A(2/3)(K/k_e)(k/k_e)^4\exp[-2(k/k_\eta)][1+(k/k_e)^2]^{-17/6} \tag{14}$$

where K is the turbulent kinetic energy, A is a numerical constant, k_e is the wave number of maximum energy, and $k_\eta=\epsilon^{1/4}\nu^{-3/4}$ is the Kolmogorov wave number. The constants A and k_e can be determined by equating the integral energy and the integral length scale derived from Eq. (14) to the RANS quantities K and $L_T=c_1u'^3/\epsilon$, respectively, $u'=\sqrt{2K/3}$ being the isotropic turbulent velocity and c_1 the first tuning parameter of the method. This provides $A\simeq 1.453$ and $k_e=0.747/L_T$. The parameter c_1 allows us to tune the RANS turbulent length scale u'^3/ϵ to the integral length scale of the large-scale eddies. Its value is, by definition, close to 1, but its optimal value depends on the turbulent flow structure and conditions and on the RANS turbulence model. In the present work, numerical experiments have been carried out in order to investigate the sensitivity of the noise prediction to the value of c_1.

The stochastic velocity perturbation field can be now generated by choosing probability density functions for all the random variables involved in Eq. (13). These are the angles φ_n and θ_n defining the direction of the wave vector $\mathbf{k}_n$, as sketched in Fig. 1; the angle α_n defining the direction of the unit vector $\boldsymbol{\sigma}_n$ in a plane orthogonal to $\mathbf{k}_n$; and finally the phase angle ψ_n. By requiring that the wave vector is uniformly distributed in the 3-D wave-number space provides the following probability densities:

$$\mathcal{P}(\varphi_n)=(2\pi)^{-1},\quad\text{with}\quad -\pi\le\varphi_n\le\pi \tag{15}$$

$$\mathcal{P}(\theta_n)=\cos(\theta_n)/2,\quad\text{with}\quad -\pi/2\le\theta_n\le\pi/2 \tag{16}$$

Analogously, by supposing that the $\boldsymbol{\sigma}_n$ vector is uniformly distributed in the plane normal to $\mathbf{k}_n$ yields

$$\mathcal{P}(\alpha_n)=(2\pi)^{-1},\quad\text{with}\quad -\pi\le\alpha_n\le\pi \tag{17}$$

Finally, the phase angle ψ_n is also supposed to be uniformly distributed in the 2π range; that is,

$$\mathcal{P}(\psi_n)=(2\pi)^{-1},\quad\text{with}\quad -\pi\le\psi_n\le\pi \tag{18}$$

The duration and sampling frequency of the synthetic velocity signals are defined on the basis of the prescribed minimum and maximum frequencies to be covered by the CAA analysis. In particular, in order to prevent aliasing effects, the time step is such that twice the value of the prescribed maximum frequency can be achieved. Interestingly, a number of stochastic realizations of the source field can be computed by seeding the random generators. For each of them, the radiated noise is computed and results are finally averaged in order to track statistically converged noise spectra.

The first original aspect of the present SNGR formulation is that the extremes of the wave-number interval are related, at each node of the CFD mesh, to the value of the wave number k_e through the relationships $k_1=c_2k_e$ and $k_{N_F}=\min(c_3k_e,k_\eta,2\pi/(N_w\Delta_i))$, where $\Delta_i=\max(|\mathbf{U}_i\cdot(\mathbf{x}_j-\mathbf{x}_i)|/U_i$ is the maximum distance between node i and its neighboring stencil nodes j, projected in the direction of the local mean-flow velocity $\mathbf{U}_i$; and N_w is the number of

grid points per the Fourier component, set to 6 in the present work, as suggested by Bailly and Juvé [7]. The constants c_2 and c_3 are two additional tuning constants of the stochastic model. The use of an adaptive wave-number interval allows reducing of the number of Fourier modes. Furthermore, in order to obtain a better discretization of the energy spectrum at the lower energy-containing Fourier modes, a logarithmic distribution of the k_n values is used; that is, $k_n = \exp[\ell_n(k_1) + D(n-1)]$, with $D = [\ell_n(k_{N_F}) - \ell_n(k_1)]/(N-1)$. The energy spectrum $E(k)$ is integrated over each band n to obtain the magnitude of the velocity component $\hat{u}_n$ by discretizing the interval D in a number of constant subintervals, from the value $k_n^- = \exp[\ell_n(k_1) + D(n-1.5)]$ up to the value $k_n^- = \exp[\ell_n(k_1) + D(n-0.5)]$.

The second original aspect of the present SNGR formulation is related to the approach used to prescribe the two-point space correlation of the velocity fluctuations at each node of the CFD mesh. The simplest approach, used for instance in [6], would consist in segmenting the bounding box of the active source region in square paths with edges equal to the average value of the correlation length over the whole source region. Then, a set of stochastic angles are sampled in each patch and these values are finally attributed to all the mesh nodes falling in the patch. The main pitfall of this approach is that the correlation length is the same over all the source region, and therefore does not account for the local Reynolds stresses and size of the turbulent structures. A different approach has been used in this work, which consists of the following two steps.

In the first step, the RANS correlation lengths

$$l_k^i = |-0.18(K^2/\epsilon)\partial U_k/\partial x_k + 2K/3)|^{3/2}/\epsilon$$

along the three Cartesian directions, each one denoted by subscript k, are evaluated at each node i of the CFD mesh. Then, the list of nodes is ordered from the smaller value of the geometric mean value $\tilde{l} = (l_1 l_2 l_3)^{1/3}$ to the larger ones. Then, starting from the first node i in the ordered list, coherent turbulent blobs are built by attributing an incremental blob index to each node of the CFD mesh that falls in the ellipsoid centered at node i and having semiaxes equal to l_k^i. Only nodes that have not already been attributed to a previous blob can be attributed to the current blob. Finally, a number of sets of random angles φ, θ, α, and ψ equal to the number of individuated blobs is generated and each set is attributed to all the nodes falling inside a blob.

In the second step, the four fields of random angles are smoothed using the following Gaussian filter:

$$\tilde{R}_i = \frac{\sum_j^{J^i} \exp\left[\ell_n(c_4)\sum_{k=1}^3 \left(\frac{x_k^j - x_k^i}{l_k^i}\right)^2\right]\tilde{r}_j}{\sum_j^{J^i} \exp\left[\ell_n(c_4)\sum_{k=1}^3 \left(\frac{x_k^j - x_k^i}{l_k^i}\right)^2\right]} \tag{19}$$

where J^i denotes the number of nodes in the mesh stencil around node i, $\tilde{r}_j$ denotes the value of the generic stochastic quantity at node j, and $\tilde{R}_i$ is the corresponding filtered value at node i. This filtering procedure can be applied recursively. The constant c_4 in Eq. (19) denotes the size of the Gaussian filter ($0 < c_4 < 1$) and constitutes the fourth and last tuning constant of the model. A vanishing nonzero value of c_4 has a no-filtering effect. The idea of filtering a random field to control the spatial correlation is similar to the one used in the RPM method [9–11] and derived from the work of Careta et al. [5].

Figure 2 show samples of the stochastic angle Ψ for the jet case discussed in Sec. IV and for the airfoil case discussed in Sec. VI. The active source region of the jet extends from 1 to 23 nozzle diameters from the nozzle exit in the axial direction. The average correlation length over the whole source volume is about 38.2% of the jet

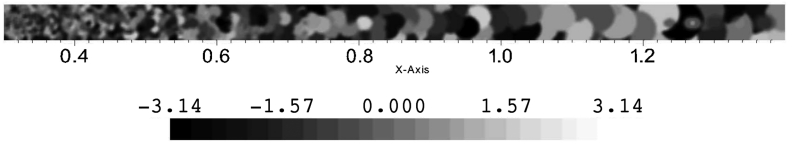

a) Jet flow: contour plots of Ψ

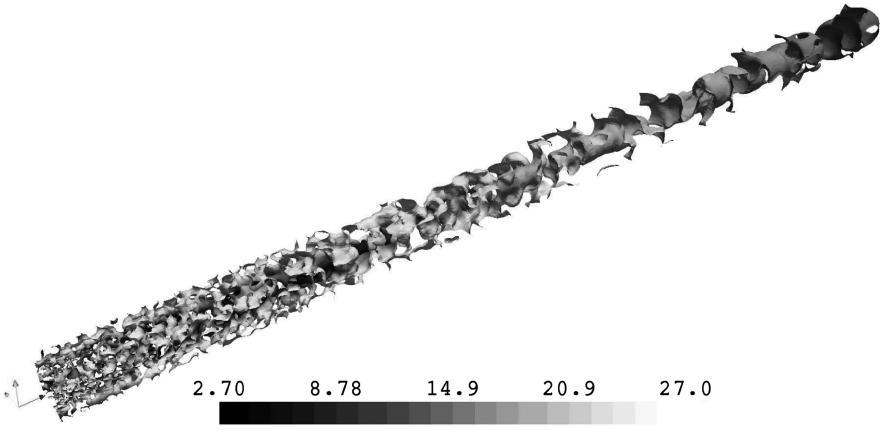

b) Jet flow: isosurface Ψ = 0

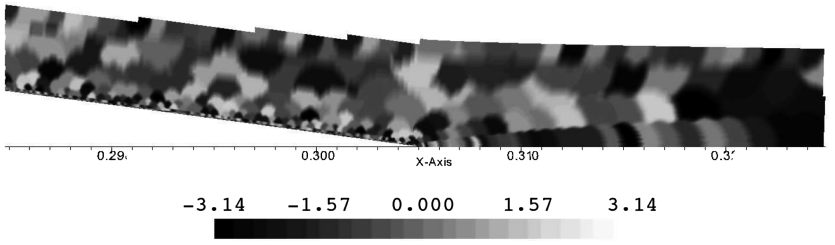

c) Airfoil flow: contour plots of Ψ

Fig. 2 Sample fields of the stochastic angle Ψ [deg] and isosurface Ψ = 0 for the jet colored by the turbulent velocity [m/s].

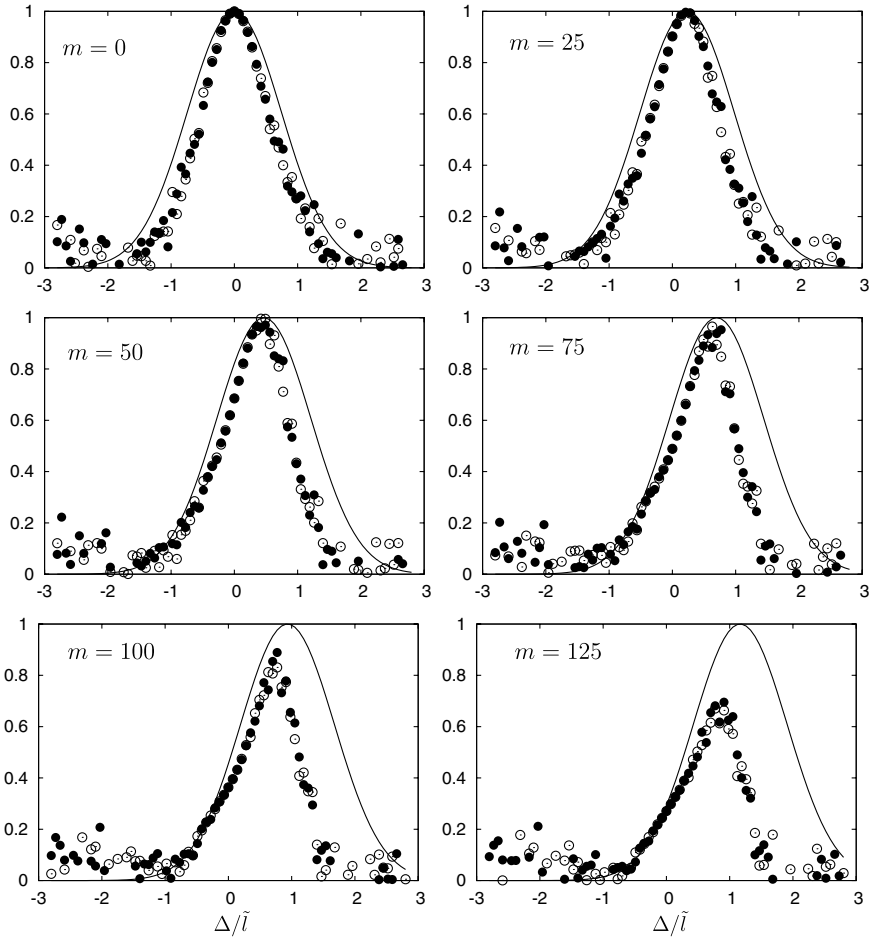

Fig. 3 Longitudinal velocity correlation function $R(\Delta/\tilde{l}, \tau^m)$. Uniform K distribution (filled circles), parabolic K distribution (open circles), and theoretical formula (lines).

diameter ($Re_D = 5.8 \times 10^5$, $M_j = 0.585$). The active source region of the airfoil extends from −6.56 to 6.56% of the chord in the streamwise direction about the trailing edge. The average correlation length over the whole source area is about 0.26% of the airfoil chord ($Re_c = 1.46 \times 10^6$, $M_a = 0.208$). More details about the jet and airfoil source regions are provided in Secs. IV and VI, respectively. A qualitative analysis of the random field shows that a texture composed by several blobs of variable size has been generated by the algorithm. For the jet case, the blobs are smaller close to the nozzle and larger downstream. This is particularly evident in the isosurface $\Psi = 0$ shown in Fig. 2b. For the airfoil case, the blob size is proportional to the distance from the wall. A quantitative analysis of the impact of a nonuniform blob size distribution on the jet-noise prediction is carried out in Sec. IV.

The time dependence in Eq. (13) is accounted for by the mean-flow convective effects, according to a frozen turbulence convection hypothesis. To reproduce the kinematics of small-scale turbulent eddies, an explicit time dependence can be added to the argument of the cosine function [7]. A different approach has been used in this paper, which is derived from the stochastic vortex shedding model described in [22]. The main idea is that the kinematics of small-scale turbulence can be represented through a random perturbation of the phase angle Ψ in Eq. (13), say $\tilde{\Psi} = \tilde{\Psi} + \Delta\tilde{\Psi}$, where the random quantity $\Delta\tilde{\Psi}$ is supposed to have a Gaussian probability density, and the angle Ψ denotes the random value attributed to the blob. Following the analysis of [22], the correlation coefficient between the nth Fourier mode of one velocity component $u'(\mathbf{x}, \mathbf{t})$ at two points separated by the distance Δ reads

$$\rho(\Delta) = \mathcal{E}[\cos(\Delta\tilde{\Psi})] = \exp\left(-\frac{w}{2}\right) \tag{20}$$

where $\mathcal{E}[\,]$ denotes the expected value, and w is the variance of the distribution $\Delta\tilde{\Psi}$. The variance can be related to the distance from the centroid of the blob. To recover a Gaussian correlation coefficient with correlation lengths l_k along the kth coordinate direction, the variance must be a quadratic function of the distance from the blob centroid; that is,

$$w(\mathbf{x}_j) = \frac{\pi}{2}\sum_{k=1}^{3}\left(\frac{x_k^j - x_k^i}{l_k^i}\right)^2 \tag{21}$$

where j is a node of the blob centered at node i.

To check the space-time correlation of the velocity fluctuations, two simple numerical experiments have been carried out. A square domain of edge equal to $6\tilde{l}$ has been discretized with 81 points per direction. Only one circular blob of radius $3\tilde{l}$ has been generated in the center of the domain. The frequency range of the analysis is [20 Hz:2 kHz]. The mean-flow convection velocity is such that the distance $\tilde{l}$ is covered in 100 time steps $\Delta t = (4f_{\max})^{-1}$. In a first experiment, the flow is uniform throughout the domain, whereas in a second experiment, the turbulent kinetic energy K varies parabolically along the x_1 direction, with a minimum at the blob center and a maximum at the boundaries of the domain. The minimum value of K is equal to the value in the first experiment, while the maximum is 30% higher than the minimum. The goal of this second experiment is to investigate the effect on the velocity correlation due to the variation of the wave-number interval over the blob. The following discrete form of the space-time longitudinal velocity correlation is plotted in Fig. 3:

$$R(\Delta, \tau^m) = \frac{\sum_{j=N/4+1}^{j=3N/4} \sum_{k=1}^{3} u_k(\mathbf{x}, t^j) u_k(\mathbf{x} + \Delta\hat{i}, t^j + \tau^m)}{\sum_{j=N/4+1}^{j=3N/4} \sum_{k=1}^{3} u_k(\mathbf{x}, t^j) u_k(\mathbf{x}, t^j)}$$
$$\text{for } m = -N/4, \ldots, N/4 \tag{22}$$

where $t^j = j\Delta t$ and $\tau^m = m\Delta t$. The results have been obtained by using the model parameters $c_1 = 1$, $c_2 = 0.1$, $c_3 = 10$, $c_4 = 0.9$, and $N_F = 50$, and by averaging the velocity correlations over 20 samples. The computed correlation is compared with the theoretical expression of the longitudinal correlation; that is,

$$R^T(\Delta, \tau^m) = \exp[-0.25\pi(\Delta - U\tau^m)^2/\tilde{l}^2]$$

It is interesting to observe that the theoretical Gaussian space correlation is reproduced at zero time lag. For nonzero time lags, the correlation function becomes unsymmetrical and its maximum decreases at increasing values of τ, thus reproducing a time decorrelation effect. It is worthwhile to remark that the correlation is not affected by the K distribution. Therefore, the spatial correlation is not significantly affected by the variation of the wave-number interval over the blob.

IV. Jet-Noise Prediction and Experiment

In this section, the noise source model described in Sec. III is validated against jet-noise measurements carried out at the École Centrale de Lyon in the framework of the European Union (EU) Seventh Framework Project OPENAIR (optimization for low environmental noise impact aircraft). The nozzle used in the experiments was designed in the EU Fifth Framework Project JEAN (jet exhaust aerodynamics and noise). The exhaust diameter is about $D_j = 0.05$ m, and the profile is shown together with the CFD mesh in Fig. 4. Some information about the JEAN project and the nozzle can be found in [23]. The goal of the experiments in the OPENAIR project was to investigate the benefits associated with an active jet-noise control system. The results shown in this paper correspond to the reference configuration without control.

The experiments have been conducted in the large anechoic wind tunnel of the École Centrale de Lyon. The room length, width, and height are $10 \times 9 \times 8$ m, respectively. The jet is powered by a centrifugal compressor and, after compression, the air is electrically heated by a set of resistances in order to maintain the temperature of the expanded jet close to room temperature. The jet Mach number is monitored by means of a total pressure probe located inside the duct 3 m upstream the nozzle exit. The results used for the validation of the noise source model, originally presented in this paper, correspond to a nominal Mach number at the nozzle exit $M_j = 0.585$. The Reynolds number based on the nozzle diameter is 5.8×10^5 ($p_a = 98,388$ Pa, $T_a = 298$ K). Noise measurements have been made with a circular rack of 13 microphones (model type PCB-ref.377B01) located 2 m from the nozzle exit and oriented in the direction of the nozzle exit center. Average spectra have been computed from 60 blocks of 1 s duration, with a sampling frequency of 102,400 Hz.

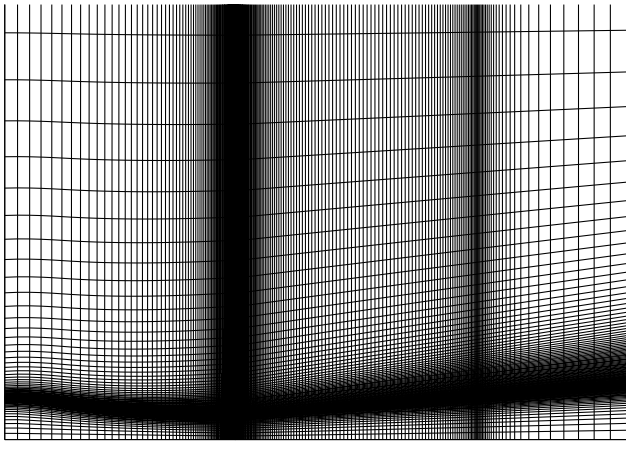

Fig. 4 Zoom view in the nozzle region of the CFD mesh used for the RANS jet flow simulation.

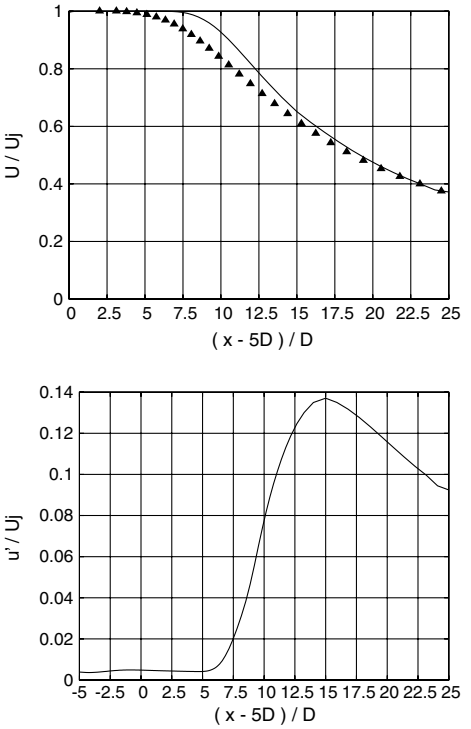

Fig. 5 RANS solution: centerline velocity (top) and turbulent kinetic velocity $u' = \sqrt{2K/3}$ (bottom) referred to the centerline velocity at the nozzle exit U_j.

The jet flow simulation has been carried out using the CFD software Fluent by ANSYS. A pressure-based second-order upwind scheme has been employed to converge fully coupled RANS equations with turbulence accounted for through a $K - \omega$ SST model. The mesh extends from 0 to 30 nozzle diameters D in the axial direction x, the nozzle being located at $x = 5D$. The external mesh radius is $10D$. A view of the mesh in the nozzle region is shown in Fig. 4. For the scopes of the present computation, the external profile of the nozzle has been arbitrarily defined. The connector at the nozzle exit has been discretized with 60 points, the maximum and minimum grid spacing being 3.75×10^{-3} and 5.55×10^{-7} m, respectively. At the nozzle inlet, a mass flow rate of 0.457239 kg/s has been imposed at a static pressure of 98,388 Pa, and the turbulent intensity and viscosity ratio have been set to 1% and 10, respectively.

Figure 5 shows the jet centerline velocity and turbulent kinetic velocity $u' = \sqrt{2K/3}$ referred to the centerline velocity at the nozzle exit $U_j = 206.1$ m/s. Contour plots of the axial velocity and turbulent kinetic energy are shown in Fig. 6. The laminar core of about $7D$ and the decay of the centerline velocity are fairly good agreement with the experimental results reported in [24] for a jet

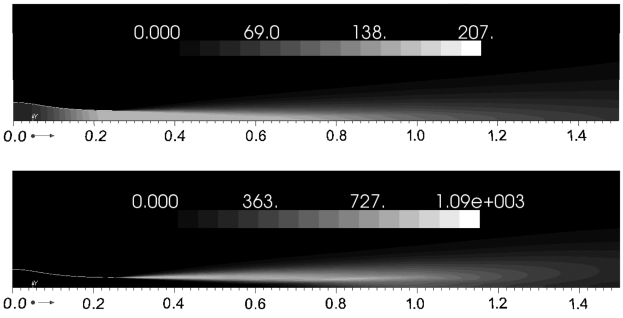

Fig. 6 RANS solution: contour plots of the axial velocity [m/s] (top) and turbulent kinetic energy [m^2/s^2] (bottom).

Table 1 Test case matrix of the SNGR jet-noise prediction

Case	c_1	c_2	c_3	c_4	N_F	Description
1	2	0.1	10	0.9	50	Reference case
2	1.5	0.1	10	0.9	50	Influence of c_1
3	2.5	0.1	10	0.9	50	Influence of c_1
4	2	0.01	10	0.9	50	Influence of c_2
5	2	0.1	100	0.9	50	Influence of c_3
6	2	0.1	10	0.5	50	Influence of c_4
7	2	0.1	10	0.1	50	Influence of c_4
8	2	0.1	10	0.9	25	Influence of N_F
9	2	0.1	10	0.9	10	Influence of N_F
10	2	0.1	10	0.9	50	Effect of [$k1$:k_{N_F}] variation over each blob
11	2	0.1	10	0.9	50	Effect of [$k1$:k_{N_F}] variation over source region
12	2	0.1	10	0.9	50	Effect of [$k1$:k_{N_F}] variation over source region
13	2	0.1	10	0.9	50	Effect of blob volume variation

Mach number $M_j = 0.6$ and Reynolds $Re_D = 1.7 \times 10^6$. The predicted laminar core length is higher than the experimental value. This has been estimated from the plot reported in [24] to be about $5D$. The higher Mach and Reynolds numbers in the experiments can justify part of the overprediction, but it can be reasonably expected that a finer computational mesh, different turbulence levels, and boundary-layer conditions at the nozzle inlet, and perhaps different turbulence models with tuned parameters [25], can reduce the discrepancy, but this is beyond the scopes of the present work. The centerline turbulent kinetic velocity is maximum at about $15D$, and this is in agreement with the DNS prediction of Freund [26] ($M_j = 0.9$, $Re_D = 3600$) and the LES prediction of Bogey and Bailly [27] ($M_j = 0.9$, $Re_D = 4 \times 10^5$).

To compute the stochastic noise sources, the axisymmetric CFD solution has been initially projected on a 3-D domain: a brick with edges $1.1 \times 0.05 \times 0.05$ m discretized with $650 \times 30 \times 30$ points. The domain spans from $x = 0.3$ m to $x = 1.4$ m (the nozzle exit is at $x = 0.25$ m). Then, from this nominal source region, cells with values of mean velocity or turbulent kinetic energy lower than 1% of the corresponding maximum values have been automatically set off. The active source region, corresponding to the set of parameters of case 1 in Table 1, is shown in Figs. 2a and 2b. The noise has been computed directly from the Fourier transform of the nonlinear Lamb vector field by using an integral solution of Powell's equation. Integration by parts is exploited in order to transfer the divergence operator from the Lamb vector to the Green function ($p' = -\int \mathcal{L}'' \cdot \nabla G \, dV$). The advantage of this approach is twofold:

1) The same source term as for the FEM propagation is used for the analytical propagation.

2) Only first-order derivatives of the velocity fluctuations $\mathbf{u}'$ are performed to compute the vorticity fluctuations $\boldsymbol{\omega}'$, and these derivations are carried out analytically using Eq. (13).

The noise has been computed at seven microphones located on a circular arc of 2 m radius, centered at the nozzle midpoint, from 30 (downward) to 150 deg, every 20 deg. For all the computations, a unitary vortex convection velocity ratio ϱ has been assumed, the analyzed frequency range is [0.1 kHz:20 kHz], and the noise spectra have been averaged over 10 samples.

A parametric study has been initially carried out in order to investigate the influence of the model parameters ($c_1, \ldots, c_4$ and N_F) on the noise prediction. Then, the benefits associated with the procedures proposed in this paper to define the wave-number interval and to build coherent blobs of variable size have been examined. The whole test case matrix is reported in Table 1. The first case in the table is the one for which a better agreement between prediction and measurements at 90 deg has been obtained. This case has therefore been used as a reference case throughout this section to compare both $\frac{1}{3}$-octave and fine-band spectra. Notice that the optimal value of the parameter c_1 is 2, while the value experimentally found by Fleury et al. [28] is 1. The origin of this difference is not clear at the present stage of the research.

Figure 7 shows results for three different values of the integral length scale constant c_1. This parameter has the effect of shifting the frequency of maximum noise. In fact, higher values of c_1 correspond

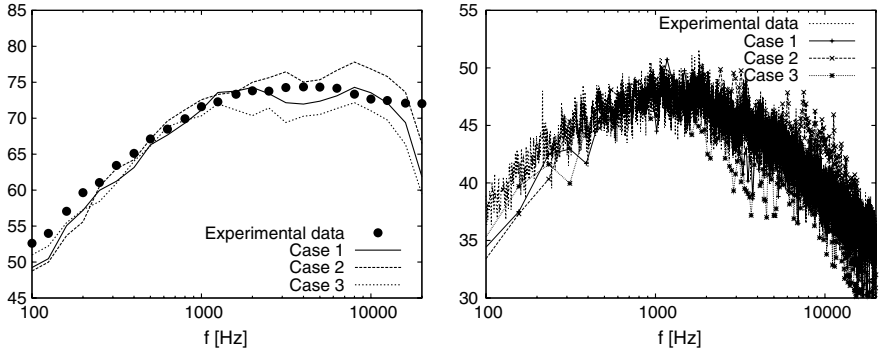

Fig. 7 Jet-noise prediction: influence of the integral length scale constant (c_1). SPL [dB] in $\frac{1}{3}$-octave bands on the left, and power spectral density (PSD) [dB/Hz] on the right.

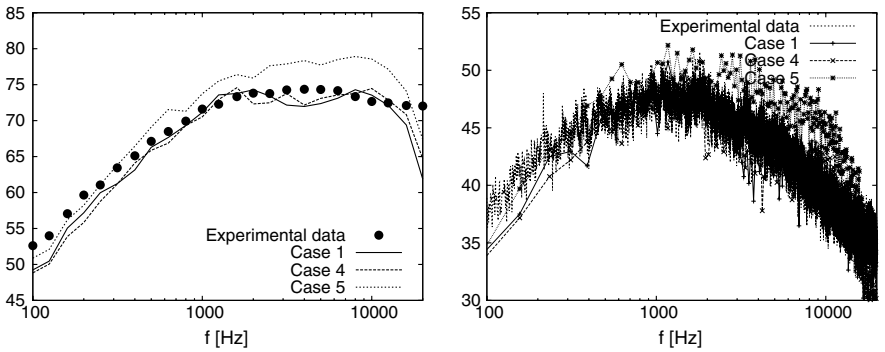

Fig. 8 Jet-noise prediction: influence of the minimum and maximum wave numbers (c_2 and c_3). SPL [dB] in $\frac{1}{3}$-octave bands on the left, and PSD [dB/Hz] on the right.

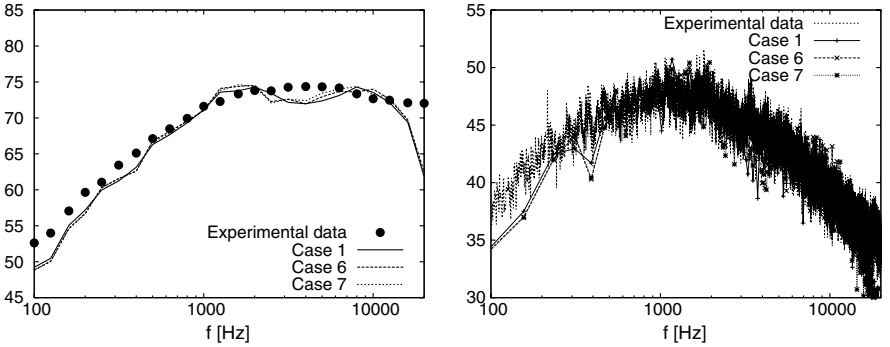

Fig. 9 Jet-noise prediction: influence of the Gaussian filter size (c_4). SPL [dB] in $\frac{1}{3}$-octave bands on the left, and PSD [dB/Hz] on the right.

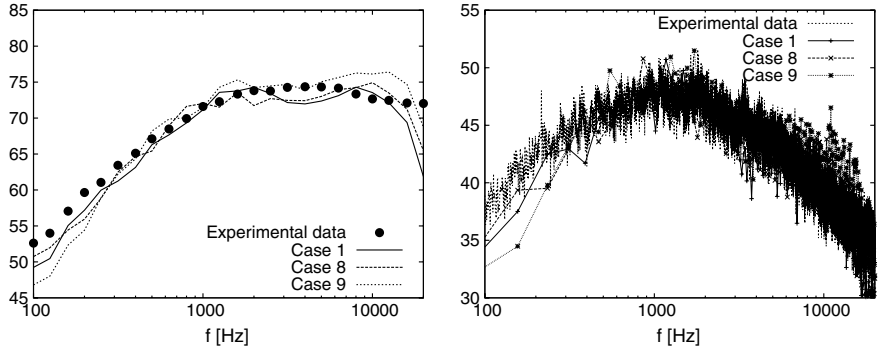

Fig. 10 Jet-noise prediction: influence of the number of Fourier modes (N_F). SPL [dB] in $\frac{1}{3}$-octave bands on the left, and PSD [dB/Hz] on the right.

to lower values of k_e, and thus to lower values of the maximum noise frequency. In fact, decreasing the value of c_1 from 2 to 1.5 increases the maximum sound pressure level (SPL) to about 3 dB, whereas increasing its value from 2 to 2.5 reduces the maximum SPL to about 2 dB. The value $c_1 = 2$ yields a good agreement with the experimental data, up to a frequency of about 12 kHz. At higher frequencies, the numerical results exhibit a rapid drop that is due to the cutoff of the maximum wave number due to the grid constraint $k_{N_F} \leq 2\pi/(N_w\Delta)$.

Figure 8 shows results for three different wave-number intervals. As described in Sec. III, the minimum and maximum Fourier mode wave numbers are defined, at each grid point, through the parameters c_2 and c_3. Reducing the minimum wave number by a factor 10 has not had a significant effect on the prediction (less then 1 dB), and this is mainly due to the fact that the same number of Fourier modes has been used for a broader frequency interval. Conversely, increasing the maximum wave number by a factor 10 results in overpredicted noise levels by about 5 dB.

Figure 9 shows results for three different values of the Gaussian filter parameter c_4. Varying the parameter from 0.9 to 0.1 affects the SPL by less than 2 dB. This is not surprising if one considers that, in the present formulation, the spatial correlation is prescribed through the blob texture and that the Gaussian filtering has only the effect of smoothing the random variables between adjacent blobs.

A model parameter that has a great impact on the computation performances of the SNGR method is the number of Fourier modes. It is therefore very interesting to check the effect of this parameter on the prediction. Figure 10 shows results for three different values of N_F. The solution computed with 25 modes differs from the reference solution computed with 50 modes by less then 2 dB, while the computational time is 67% of the reference one. The solution computed with 10 modes differs from the reference solution by less then 4 dB, while the computational time is 43% of the reference one.

One of the recognized problems with stochastic models based on Fourier modes is that the spatial dependence of the random variables can be responsible for a too high turbulence decorrelation and numerical discontinuities. In the present approach, the concept of a coherent blob has been introduced in order to control the spatial correlation, whereas the numerical discontinuities are prevented by operating a Gaussian smoothing on the random fields. Moreover, since the vorticity fluctuations are computed analytically from the Fourier series of the velocity fluctuations, and since the nonlinear Lamb vector field, and not its divergence, is integrated in weak-form [see Eq. (9)], no issue is associated with the continuity of the random variables. Concerning the effects on the spatial correlation, it can be reasonably expected that the variation of the wave-number intervals inside each blob, and consequently the variation of the discrete frequencies between neighboring points, may promote a certain spatial decorrelation. Although the elementary tests described in Sec. III have demonstrated that a proper spatial correlation is also achieved in the case of a significant variation of the wave-number interval over the size of a single blob, it is interesting to assess the influence of such a variation on the jet-noise prediction. Figure 11 shows a comparison between the reference solution and the one obtained by forcing in each blob the values of the wave number k_1 and k_{N_F} to their values at the centroid of the blob. No improvement can be observed. Conversely, a negative effect occurs between 1 and 4 kHz, which is due to the discontinuity of the wave-number intervals between two adjacent blobs.

The standard approach used to define the wave-number intervals consists of defining the minimum wave number k_1 as a fraction of the minimum value of k_e over the whole source region and the maximum wave number k_{N_F} as the value that guarantees a minimum number of grid points per Fourier component over the whole source region [7]. A possible drawback of this approach is that, in the presence of large variations of the turbulent scales, a unique interval definition for the whole source region may not be suited to model the turbulent energy spectrum with a sufficient wave-number resolution. To investigate the influence of the wave-number interval definition, two computations have been carried out. In the first one (case 11), the minimum and maximum wave numbers k_1 and k_{N_F} have been set to the maximum value of k_1 and to the minimum value of k_{N_F} over the whole source region, respectively. In the second computation (case 12), the minimum and maximum wave numbers k_1 and k_{N_F} have been set to the minimum value of k_1 and to the maximum value of k_{N_F} over the whole source region, respectively. The results are

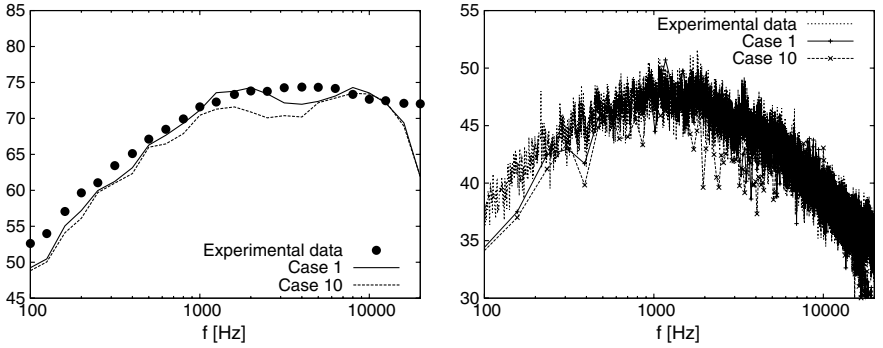

Fig. 11 Jet-noise prediction: effect of the wave-number interval variation over each blob. SPL [dB] in $\frac{1}{3}$-octave bands on the left, and PSD [dB/Hz] on the right.

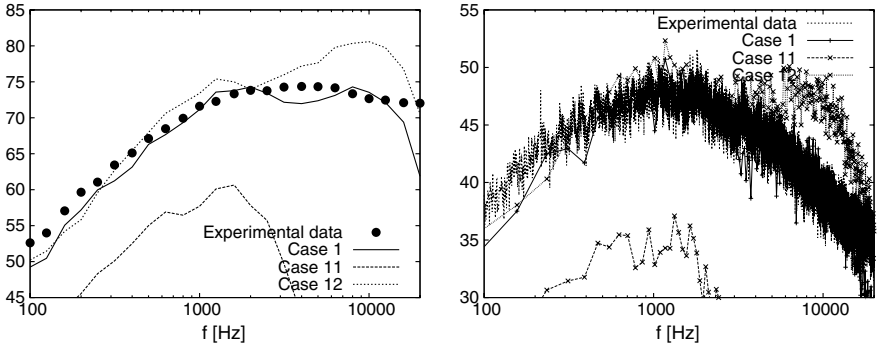

Fig. 12 Jet-noise prediction: effect of the wave-number interval variation over the source region. SPL [dB] in $\frac{1}{3}$-octave bands on the left, and PSD [dB/Hz] on the right.

shown in Fig. 12. As expected, the first solution dramatically underpredicts the noise levels, while the second one overpredicts by 6 dB the high-frequency noise levels, but this is due the violation of the wave-number cutoff condition $k_{N_F} \leq 2\pi/(N_w\Delta)$.

One of the novelties of the present SNGR model is the use of a blob texture to cluster the nodes in coherent volumes. The idea follows from the standard approach of segmenting the source region in Cartesian patches [6] of sizes equal to the average value of the correlation length over the whole source region. The main advantage of the blob clustering approach is that the size of each blob is related to the local value of the correlation length. To show the effects of the variation of the blob size, the reference results are compared in Fig. 13 to the results obtained by using blobs, and not square patches, of constant sizes equal to the average value of $\tilde{l}$. The two solutions differ by less then 2 dB.

From the results shown in Figs. 12 and 13, one may conclude that the present revision of the SNGR formulation does not constitute a significant improvement with respect to the standard formulation. However, it is important to make three remarks:

1) A jet-noise prediction is perhaps less sensitive than an airframe-noise prediction to the variation of the turbulence scales over the source region.

2) A smaller wave-number interval can be discretized with a smaller number of Fourier modes, thus resulting in faster computations.

3) The standard formulation used for the numerical tests presented in this section is indeed the present formulation with some features disabled but taking advantage of the other software implementation features.

This section is concluded by reporting the noise spectra measured and computed at seven observation angles. As shown in Fig. 14, the agreement between measurements and prediction is better at radiation angles close to 90 deg, where the noise is dominated by small-scale mixing noise. At low radiation angles, in fact, the low-frequency SPL tends to be underpredicted, up to an error of about 10 dB at 30 deg. At the same radiation angle, the frequency of maximum noise is also underpredicted. The situation is more favorable at high radiation angles: at 150 deg, the noise is overpredicted by only 5 dB, whereas

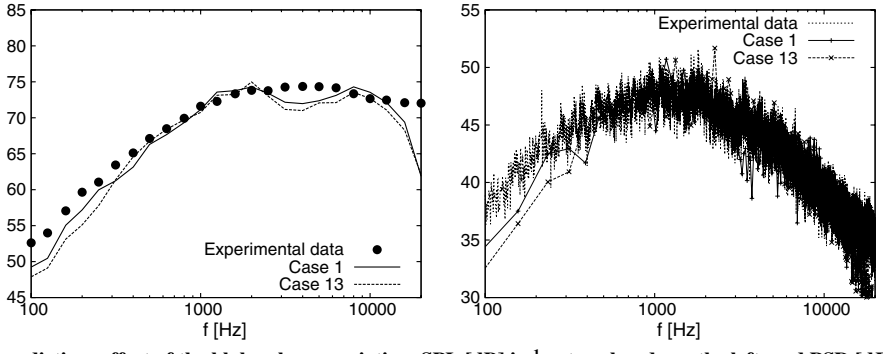

Fig. 13 Jet-noise prediction: effect of the blob volume variation. SPL [dB] in $\frac{1}{3}$-octave bands on the left, and PSD [dB/Hz] on the right.

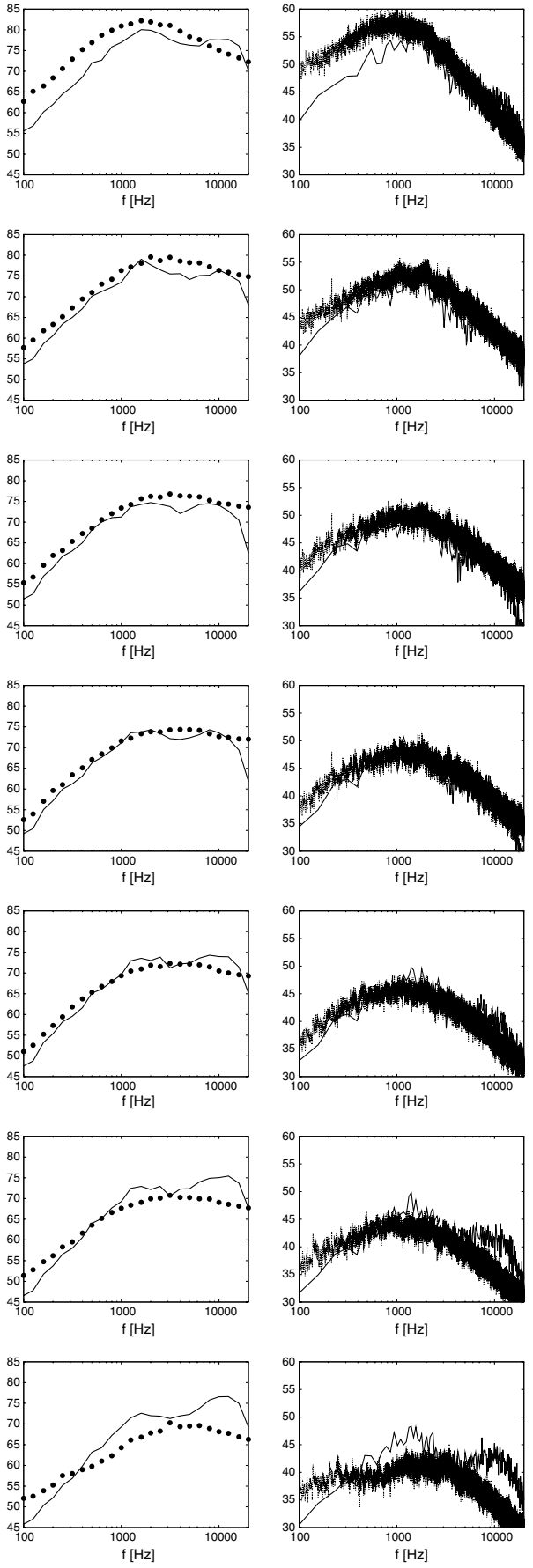

Fig. 14 Validation of the jet-noise prediction at different radiation angles, from 30 (top) to 150 deg (bottom), every 20 deg. Left column: $\frac{1}{3}$-octave bands SPL [dB] (experimental data plotted with symbols), and right column: PSD [dB/Hz] (experimental data plotted with dashed line).

the predicted frequency of maximum noise is in quite good agreement with the experimental value.

V. Airfoil Computational Fluid Dynamics Results

In this section, CFD results are presented for a set of validation cases selected from the test report by Brooks et al. [15]. Emphasis is given to the boundary-layer quantities close to the trailing edge, since these are expected to have a major impact on the far-field noise spectra. In particular, the boundary-layer values used in the semianalytical model described in the Appendix are reported. A NACA-0012 airfoil of chord $c = 0.3048$ m at a zero angle of attack and four values of the freestream velocity U_a have been considered: 31.7, 39.6, 55.5, and 71.3 m/s. The turbulent transition is not triggered numerically, and the acoustic results are compared with the natural transition cases of [15]. Since the location of the transition point affects the boundary-layer properties at the trailing edge, it is expected that the comparison between the computed boundary-layer quantities and the measured ones provides a confidence level of the predicted transition point.

Computations have been carried out using the CFD software Fluent by ANSYS. A pressure-based second-order upwind scheme has been employed to converge fully coupled RANS equations with turbulence accounted for through a $K-\omega$ SST model in transitional flow modality. The turbulence level and length scale prescribed at the upstream boundary are 0.5% and 0.1 m, respectively. Because of the lack of information about the wind-tunnel turbulence level in [15], these values have been arbitrarily set on the basis of the authors' experience. A hybrid computational mesh has been used with a first-cell spacing in the wall normal direction that provides the y^+ distribution plotted in Fig. 15. The maximum value of y^+ is well below the unitary value, thus ensuring a good resolution of the laminar sublayer. The natural transition cases of [15] have been reproduced. However, in order to better control the transition process, a zonal approach has been employed by forcing the flow laminarity up to 20% of the airfoil chord. As a consequence, the transition takes place naturally at $x/c > 0.2$ at different chordwise locations, depending on the freestream velocity.

The chordwise variation of the boundary-layer displacement thickness δ^*, momentum thickness θ, and wall skin friction τ_w have been extracted from the RANS solution and compared with the analytical solution of the von Kármán boundary-layer equation, obtained by using the Thwaites method for the laminar portion of the airfoil and the Head method for the turbulent portion. The two methods have been matched at the transition point predicted by the RANS simulation, without any blending or intermittence function. The boundary-layer asymptotic velocity required by the analytical methods has been obtained by solving the Laplace equation for the velocity potential using the FEM code $Opty\partial B$.

Figure 16 shows the comparison between RANS and analytical solutions. Differences can be observed around the transition point, due to the abrupt swap between the laminar and the turbulent methods in the analytical solution, and close to the trailing edge. Globally, the agreement between the two solutions is fairly good,

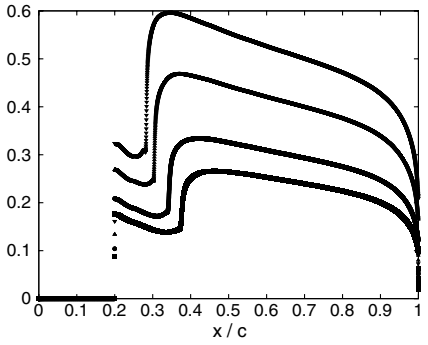

Fig. 15 y^+ distribution along the airfoil chord at different freestream velocities; $U_a = 31.7$ m/s (●: $U_a = 39.6$ m/s, ▲: $U_a = 55.5$ m/s, ▼: $U_a = 71.3$ m/s).

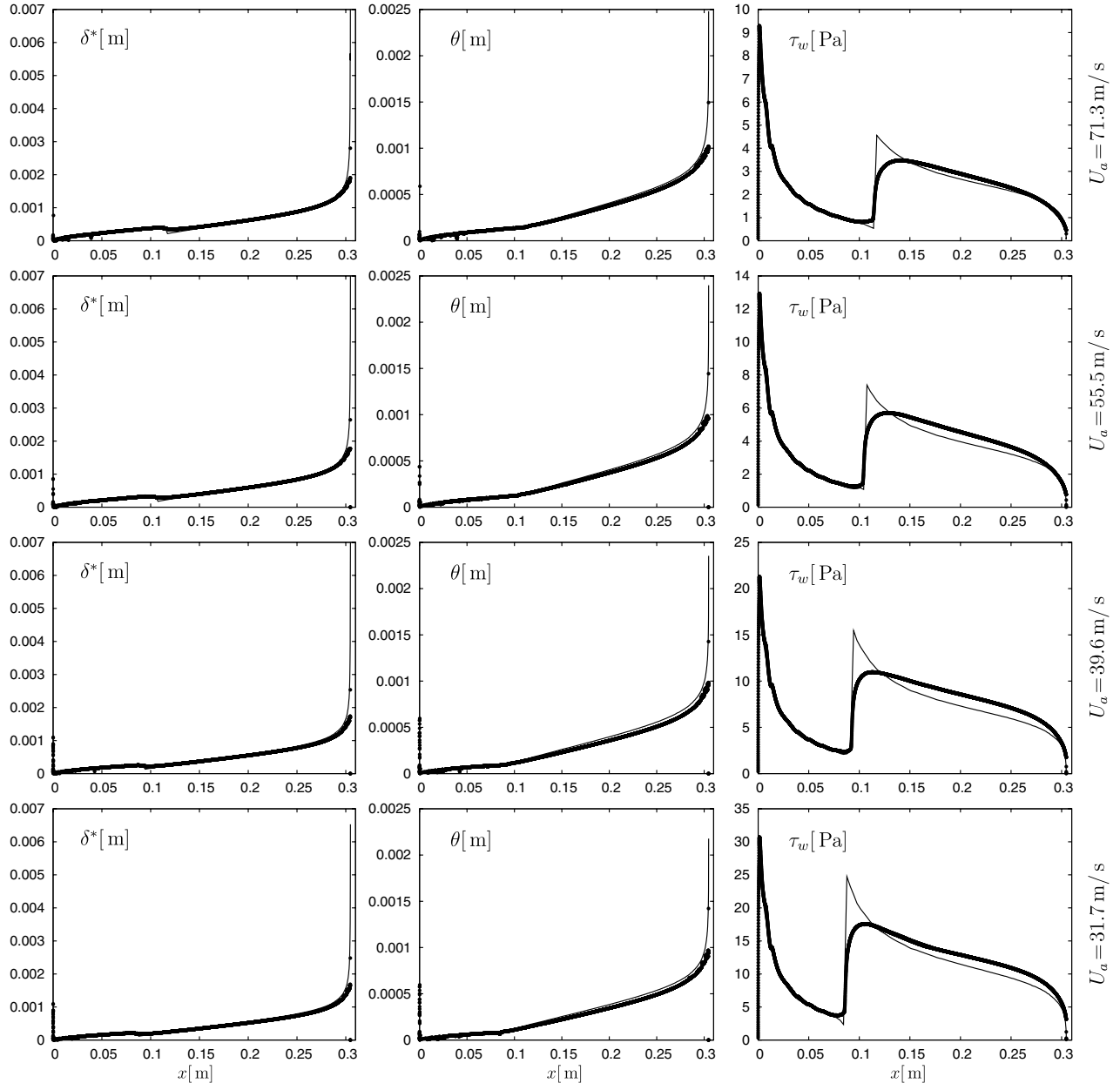

Fig. 16 NACA-0012 boundary-layer results: RANS solution (symbols), and analytical solution (lines).

providing a certain confidence about the boundary-layer resolution of the RANS solution.

Figure 17 shows a comparison between the predicted values of δ^* and θ at 99.5% of the chord and the measurements made by Brooks et al. [15], both in the case of a natural transition and a tripped boundary layer. The predicted values fall between the two sets of measurements, and the RANS results are very close to the untripped boundary-layer measurements.

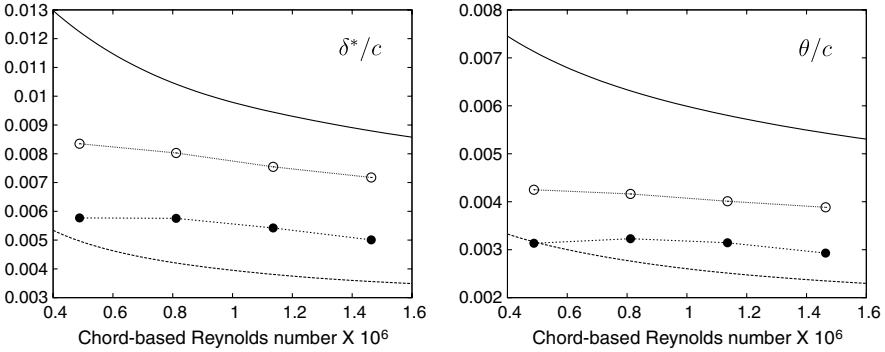

Fig. 17 NACA-0012 boundary-layer results at 99.5% of the chord. Comparison between experimental data [15], RANS solution (●), and analytical solution (○). Measurements: tripped boundary layer (solid lines) and untripped boundary layer (dashed lines).

Table 2 NACA-0012 boundary-layer RANS results at 99.5% of the chord[a]

U_a	U_e	$\delta \times 10^3$	$\delta^* \times 10^3$	$\theta \times 10^3$	τ_w	$\mathrm{d}p_0/\mathrm{d}x \times 10^5$
31.7	29.176	7.855	1.759	0.955	0.572	0.321
39.6	36.744	7.723	1.754	0.984	0.910	0.499
55.5	51.422	7.549	1.653	0.959	1.802	0.981
71.3	65.115	7.303	1.527	0.893	3.056	1.618

[a]Quantities in SI units.

The RANS boundary-layer quantities at the trailing edge used for the semianalytical noise prediction are finally collected in Table 2.

VI. Airfoil Computational Aeroacoustics Results

In this section, NACA-0012 self-noise results are presented for the four values of the freestream velocity. Computations have been carried out using the following values of the tuning parameters of the stochastic noise generation model: $c_1 = 2.0$, $c_2 = 0.1$, $c_3 = 10$, and $c_4 = 0.9$. A number $N_F = 100$ of Fourier modes has been used. It is worthwhile to remark that this setup is not specific to the addressed problem, but it has been derived through the jet-noise parametric study carried out in Sec. IV.

A number of 25 realizations of the stochastic source fields have been computed in order to achieve an appropriate level of statistical convergence of the noise spectra. As discussed hereafter, a convergence study has been carried out a posteriori to verify the convergence rate of the computed noise levels. The active source region has been located only on one side of the airfoil, as shown in Fig. 2c. The overall noise levels have then been estimated by adding 3 dB to the computed levels under the assumption of fully uncorrelated sources. Both CFD and CAA computations have been carried out using a 2-D discretization, whereas 3-D synthetic velocity fluctuations and, consequently, 3-D Lamb vectors have been computed. However, only the in-plane components of the Lamb vectors have been used for the CAA computation. Two main modeling errors are associated with this computational strategy: one is due to the wrong acoustic energy spreading, and the other one is due to the lack of information about the spanwise two-point correlation of the source terms. For a trailing-edge noise problem, these two errors can be corrected by using the formula used in [2] that relates the computed 2-D noise levels L_p^{2D} to the corresponding 3-D levels L_p^{3D}; that is,

$$L_p^{3D}(x, y, 0, \omega) = L_p^{2D}(x, y, \omega) + 10 \log\left(\frac{\mathcal{C} L U_a}{2\pi R c_a}\right) \qquad (23)$$

where $\mathcal{C}$ is an empirical spanwise correlation parameter that relates the spanwise correlation length to the freestream velocity and frequency, L is the airfoil span, and R is the observation distance. The experimental value reported by Brooks et al. [15] is $\mathcal{C} \simeq 1.5$. This value is used both to correct the 2-D CAA solutions and to compute the semianalytical solutions using the formulation reported in the appendix.

Computations are carried out from 97.65625 to 12,500 Hz, and the whole frequency range is sampled in 127 constant intervals. A structured C mesh is used that extends from −24.5 to 24.5 m along the x and y directions and consists of 709,797 nodes. The mesh size is almost constant in the radiation field, ensuring a minimum number of points per acoustic wavelength equal to about 12 at the highest frequency. PML buffers of 0.5 m thickness are used for all the computations. The multifrequency analysis is carried out by exploiting the restart capabilities of the *Opty∂B* software. In particular, the projection of the CFD solution on the CAA mesh, the computation of the three matrix factors resulting from the discretization of Eq. (10), and the cell-containing search operations for the source Dirac dipoles and the microphones are carried out only at the first run. Instead, the assembling of the governing matrix, the projection of the source Dirac dipoles, and the setup of the right-hand side, the solution of the linear system, and the interpolation of the computed solution at the microphone locations are carried out for each frequency run. The linear system is solved using the open-source library MUMPS (multifrontal massively parallel sparse direct solver) [18]. The multi-right-hand-side capabilities of MUMPS are exploited in order to manage the computation of the noise fields for the different source realizations. Using only one processor of a laptop equipped with a 2.5 GHz Q9300 Intel CPU, each frequency run requires 1 and 2 min in the case of 5 and 25 source realizations, respectively.

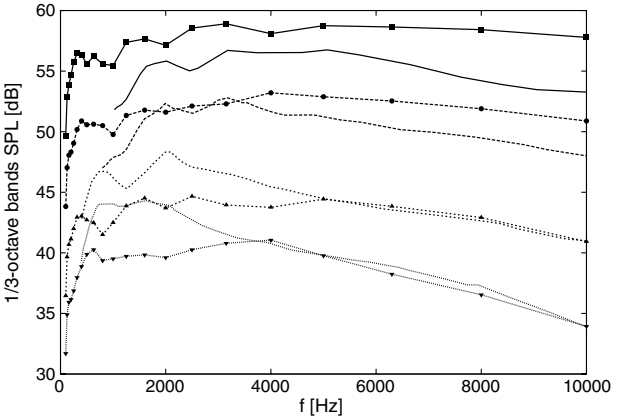

Fig. 18 Noise spectra in $\frac{1}{3}$-octave bands at 90 deg for different freestream velocities. Comparison between experimental data [15] (lines) and numerical results (lines and symbols). Solid lines: $U_a = 71.3$ m/s, long-dashed lines: $U_a = 55.5$ m/s, medium-length dashed lines: $U_a = 39.6$ m/s, and short-dashed lines: $U_a = 31.7$ m/s.

The active source region shown in Fig. 2c is defined by prescribing a rectangular bounding box about the trailing edge that extends over 0.04 and 0.01 m along x and y, respectively. Then, the cells of the CFD mesh are filtered out at 1% of the maximum mean-flow velocity and 1% of the maximum turbulent kinetic energy in the source region. The resulting number of active source cells for the $U_a = 71.3$ m/s case is 39,500. The CPU time required to compute 25 source field realizations in the addressed frequency range, with an antialiasing factor equal to 2, is about 330 min using the aforementioned computational equipment. The size of the active source region has been determined by considering boxes of increasing size in both directions and by checking the convergence of the overall SPL (OASPL) at the 90 deg microphone for the higher freestream velocity case.

Figure 18 shows a comparison between the computed and the measured noise spectra in $\frac{1}{3}$-octave bands for a microphone located at 90 deg with respect to the airfoil chord, at the same streamwise

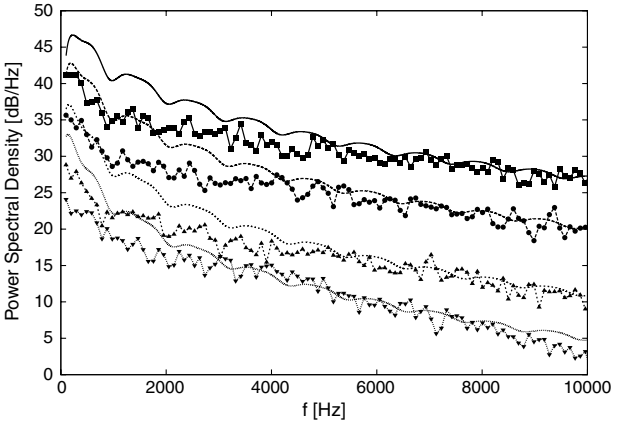

Fig. 19 Noise power spectral densities at different freestream velocities. Comparison between semianalytical (lines) and numerical results (lines and symbols). Solid lines: $U_a = 71.3$ m/s, long-dashed lines: $U_a = 55.5$ m/s, medium-length dashed lines: $U_a = 39.6$ m/s, and short-dashed lines: $U_a = 31.7$ m/s.

Table 3 OASPLs at 90 deg[a]

U_a	$Opty\partial B$	4.6-power law fitting	Δ_{46}
31.07	69.8	68.3	1.5
39.6	72.9	72.7	0.2
55.5	79.6	79.5	0.1
71.3	84.5	84.5	0.0

[a]Comparison between $Opty\partial B$ results and the power-law fittings OASPL $= 10\log(U_a^{4.6}) - 0.762$.

location of the trailing edge, and at a radial distance of 1.22 m. The noise levels for the highest velocity case are overpredicted up to about 5 dB at the highest frequencies. Conversely, the low-frequency noise levels are underpredicted by about 5 dB for the lowest velocity case. Globally, the agreement between numerical predictions and measurements is fair.

Figure 19 shows a comparison between the computed power spectral density for the four velocity cases and the ones computed using the semianalytical formula reported in the Appendix. The same spanwise correlation parameters used to correct the 2-D CAA noise levels have been used to carry out the semianalytical prediction [$\mathcal{C} = 1.5$ in Eq. (A1)], whereas the eddy convection velocity U_c has been supposed to be equal to 70% of the asymptotic boundary-layer velocity U_e [$\alpha = 1.43$ in Eq. (A4)]. The agreement between the two RANS-based solutions is quite satisfactory at frequencies higher than about 4 kHz. At lower frequencies, the power spectral densities are significantly different. Although the origin of this low-frequency disagreement between the two solutions is not clear, the agreement in

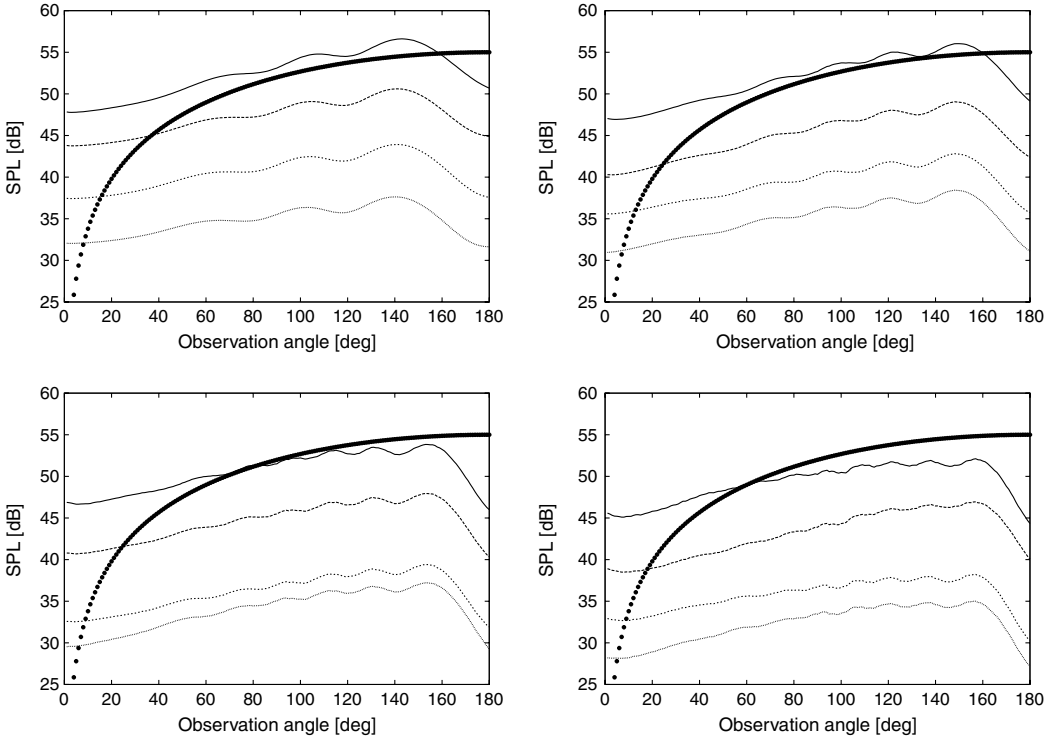

Fig. 20 SPL directivity at a distance of 1.22 m averaged over 25 stochastic realizations. Top left: $kc = 10$, top right: $kc = 15$, bottom left: $kc = 20$, and bottom right: $kc = 25$. Solid lines: $U_a = 71.3$ m/s, long-dashed lines: $U_a = 55.5$ m/s, medium-length dashed lines: $U_a = 39.6$ m/s, and short-dashed lines: $U_a = 31.7$ m/s. Comparison with a cardioid radiation pattern $20\log(\sin\theta/2) + 55$ (symbols).

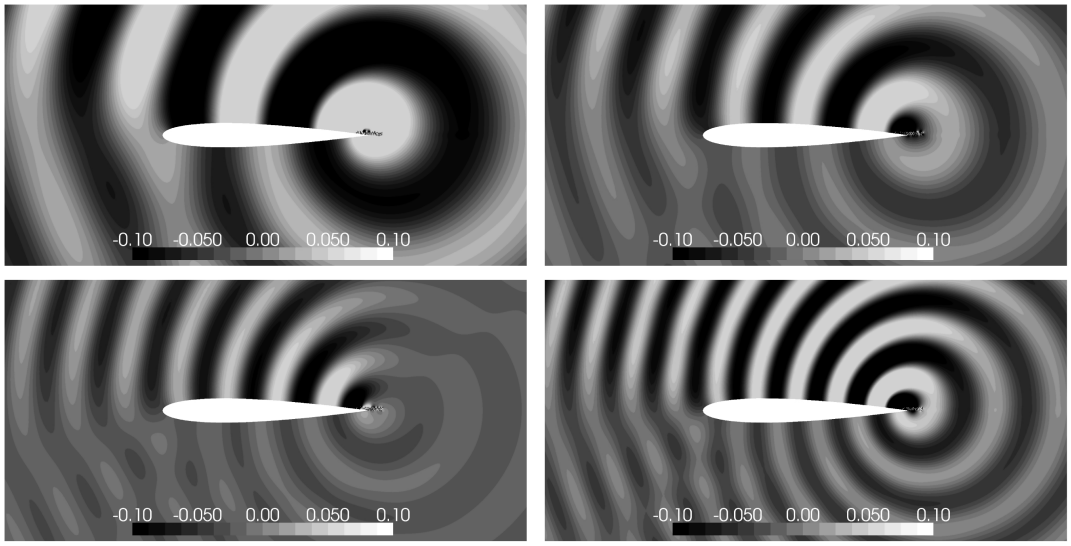

Fig. 21 Real part of the acoustic pressure for the case $U_a = 71.3$ m/s, corresponding to one of the 25 source field samples. Top left: $kc = 10$, top right: $kc = 15$, bottom left: $kc = 20$, and bottom right: $kc = 25$. The range of the contour plots has been adapted for graphical reasons.

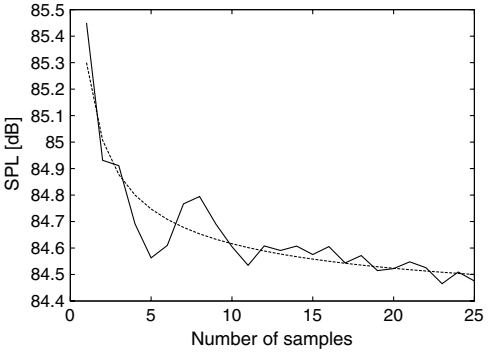

Fig. 22 SPL at an observation angle of 90 deg ($U_a = 71.3$ m/s) averaged over an increasing number of samples. Comparison of the predicted statistical convergence curve (solid line) with the theoretical rule $1\sqrt{N} + 84.3$ (dashed line).

the high-frequency regime is an important outcome of the present study, since it shows that the stochastic nonlinear Lamb vector field is consistent with the two-point wall pressure statistics computed analytically from the RANS solution.

In Table 3, the computed OASPLs are reported for the four freestream velocities and compared with a 4.6 power-law fitting. The power-law exponent of 4.6 is in agreement with the one found by Ewert et al. [2].

SPL directivities at increasing values of the chord-based Helmholtz number kc are plotted in Fig. 20. The levels have been obtained by averaging over 25 stochastic realizations, by considering only the acoustic solutions in one side of the airfoil, and by adding 3 dB to account for the opposite side of the airfoil. The interference lobes that occur in the forward radiation arc are mainly due to the leading-edge scattering effects. Conversely, the expected trailing-edge diffraction lobes are smeared out by the average over the 25 realizations and, for each realization, over the whole active source field. For all cases, the predicted directivity pattern is somehow different from what is expected for trailing-edge noise. Theoretical models for a semi-infinite flat plate predict a cardioid radiation pattern $\sin(\theta/2)$, where the vanishing noise condition at $\theta = 0$ is due to the vanishing thickness of the flat plate, whereas the maximum noise at $\theta = \pi$ is due to the infinite extension of the flat plate. Both these conditions are not fulfilled by a real airfoil. As a consequence, as shown in Fig. 20, the cardioid radiation pattern can be only partially recovered.

Near-field contour plots of the acoustic pressure at the start of the cycle for the freestream velocity $U_a = 71.3$ m/s, generated by one of the 25 stochastic source realizations at different values of the Helmholtz number, are shown in Fig. 21.

The results shown in this section have been computed by averaging the noise spectra over 25 stochastic samples. Since the computational time required to compute both the stochastic source field and the FEM solutions can be reduced by reducing the number of samples, it is worthwhile to verify a posteriori the statistical convergence of the far-field noise. The OASPL at an observation angle of 90 deg is plotted against the number of stochastic samples in Fig. 22. The numerical convergence curve is compared against the theoretical rule $1/\sqrt{N}$, showing a good agreement. Interestingly, using 25 samples instead of five results in less than a 0.2 dB of difference.

VII. Conclusions

A stochastic RANS-based aeroacoustic source model has been validated against jet-noise measurements and then used to compute the right-hand side of a second-order wave equation derived from the Howe acoustic analogy and solved in the frequency domain. A FEM discretization technique has been used, which makes straightforward the projection of the source terms from the CFD mesh to the CAA mesh. This methodology has been applied to the prediction of the broadband noise generated by the boundary-layer turbulence convected past the trailing edge of a NACA-0012 airfoil. The CAA results have been compared with literature measurements, showing a fair agreement in terms of spectral trend and velocity power law. Differences up to about 5 dB between measurements and predictions have been obtained. In addition, a verification process has been carried out by comparing the CAA results with semianalytical results computed using boundary-layer quantities extracted from the same RANS solution used in the stochastic method. A good agreement has been observed at frequencies higher than about 4 kHz, which demonstrates the capability of the stochastic model to recover the two-point statistical properties of a wall-bounded turbulent flowfield. However, significant differences between the two sets of numerical predictions have been obtained at low frequencies. The stochastic noise generation formulation is based on a revised version of the SNGR method that allows taking into account the field variation of the turbulence correlation length in the source statistics. The idea of clustering the random angles of the turbulent velocity vectors according to a coherent blob texture and then smoothing these angles through a Gaussian filter has been originally proposed. Finally, it is worthwhile to remark that a careful architectural design and optimization of the stochastic noise generation software is the crucial element for the application of the method to realistic 3-D problems.

Appendix: Semianalytical Model of the Trailing-Edge Noise

This Appendix describes the airfoil self-noise semianalytical model that has been recently implemented at the Centro Italiano Ricerche Aerospaziali and used in [29] to perform an aeroacoustic optimization of the blade of a pusher propeller. More details about the model and its validation can be found in the referred article.

A constant wing segment of chord c and span length L is considered. The freestream direction is parallel to the x axis, the trailing edge being defined by $x = 0$, $y = 0$, and $-L/2 \le z \le L/2$. Following the formulation of [30,31], the noise power spectral density can be written as

$$S_{pp}(x, y, z, \omega) = \left(\frac{\bar{k}z}{2\pi\sigma^2}\right)^2 2L\frac{\mathcal{C}U_c}{\omega}\phi_{pp}(\omega)\left|I\left(\frac{\bar{k}}{U_c}, \bar{k}_y\right)\right|^2 \quad \text{(A1)}$$

where $\bar{k} = \omega c/(2c_0)$ is the nondimensional acoustic wave number, $\sigma = \sqrt{x^2 + \beta^2(y^2 + z^2)}$ is the Prandtl–Glauert transformed distance from the trailing edge ($\beta = \sqrt{1 - M^2}$), Φ_{pp} is the wall pressure frequency spectrum, U_c is the boundary-layer eddy convection velocity, $\bar{k}_y = k_y c/2$ is the nondimensional wave number in the spanwise direction, $\mathcal{C}$ is a nondimensional constant related to the spanwise correlation length, and I is the radiation integral function. This consists of a main contribution I_1 derived from the assumption of a semi-infinite flat plate (high-frequency approximation) and a term I_2 accounting for the wave backreflection at the leading edge (finite chord length correction), for which the expressions are

$$I_1 = \frac{ie^{2iC}}{C} \times \left\{(1+i)e^{-2iC}\sqrt{\frac{B}{B-C}}E^*(2B-2C) - (1+i)E^*(2B) + 1\right\} \quad \text{(A2)}$$

$$I_2 = H\{e^{4i\bar{k}}[1 - (1+i)E^*(4\bar{k})]\}^{\varepsilon} + H[-e^{2i\Theta^-} + i(\Theta^- + \bar{k}_x + M\bar{\mu} - \bar{k})G] \quad \text{(A3)}$$

where $\bar{k}_x = k_x c/2$ is the nondimensional wave number in the streamwise direction, $M = U_e/c_0$ is the asymptotic boundary-layer Mach number, $\bar{\mu} = \omega c/(2c_0\beta^2)$,

$$E^*(\xi) = \int_0^{\xi} e^{-it}/\sqrt{2\pi t}\,\mathrm{d}t$$

is the Fresnel integral, and the notation $\{\}^{\varepsilon}$ means that the imaginary part must be multiplied by a factor $\varepsilon = 1/\sqrt{1+1/(4\bar{\kappa})}$. The other functions are defined as follows:

$$B = \bar{K}_x - M\bar{\mu} + \bar{\kappa}, \qquad C = \bar{K}_x - \bar{\mu}(x/\sigma - M)$$

$$H = \frac{(1+i)e^{-4i\bar{\kappa}}(1-\Theta^2)}{2\sqrt{\pi}(\alpha-1)\bar{k}_x\sqrt{B}}, \qquad \Theta^- = \bar{\kappa} - \bar{\mu}x/\sigma$$

$$\begin{aligned} G = {} & (1+\varepsilon)e^{i(2\bar{\kappa}+\Theta^-)}\frac{\sin(\Theta^- - 2\bar{\kappa})}{\Theta^- - 2\bar{\kappa}} \\ & + (1-\varepsilon)e^{i(-2\bar{\kappa}+\Theta^-)}\frac{\sin(\Theta^- + 2\bar{\kappa})}{\Theta^- + 2\bar{\kappa}} \\ & + \frac{(1+\varepsilon)(1-i)}{2(\Theta^- - 2\bar{\kappa})}e^{4i\bar{\kappa}}E^*(4\bar{\kappa}) - \frac{(1-\varepsilon)(1+i)}{2(\Theta^- + 2\bar{\kappa})}e^{-4i\bar{\kappa}}E(4\bar{\kappa}) \\ & + \frac{e^{2i\Theta^-}}{2}\sqrt{\frac{2\bar{\kappa}}{\Theta^-}}E^*(2\Theta^-)\left[\frac{(1-\varepsilon)(1+i)}{\Theta^- + 2\bar{\kappa}} - \frac{(1+\varepsilon)(1-i)}{\Theta^- - 2\bar{\kappa}}\right] \end{aligned} \quad \text{(A4)}$$

where $\bar{\kappa}^2 = \bar{\mu}^2 - \bar{k}_y^2/\beta^2$, $\bar{K}_x = \omega c/(2U_c)$, and $\alpha = U_e/U_c$ is the ratio between the boundary-layer asymptotic velocity and the eddy convection velocity. The wall pressure wave-number-frequency spectrum $\Phi_{pp}(\omega/U_c, k_y)$ in Eq. (A1) can be related to the wall pressure power spectral density $\phi_{pp}(\omega)$ and to the spanwise two-point coherence $\gamma(\eta_y, \omega)$ through the relationship $\Phi_{pp}(\omega/U_c, k_y) = \phi_{pp}(\omega) l_y(\omega, k_y)/\pi$, with

$$l_y(\omega, k_y) = \int_0^{\infty} \gamma(\eta_y, \omega)\cos(k_y\eta_2)\,\mathrm{d}\eta_2$$

The spanwise correlation length is assumed to be given by the Corcos formula $l_y(\omega, k_y) = \mathcal{C}U_c/\omega$.

Empirical models of the wall pressure frequency spectrum $\phi_{pp}(\omega)$ beneath a turbulent boundary layer have been proposed by several authors in the past. It is recognized that the low-frequency part of the spectrum is affected by the outer region of the boundary layer, whereas the high-frequency part is affected by the inner region. Therefore, depending on the employed normalization quantities [outer (δ^*, U_e) or inner (τ_w, ν) quantities], different formulations have been developed. Among others, Schlinker and Amiet [32] normalized the wall pressure spectrum with outer boundary-layer quantities, and Chase [33] and Goody [34] used a combination of inner and outer quantities, the second one accounting for the Reynolds number effects. In this paper, the models proposed by Schlinker and Amiet [32] have been used.

The model proposed by Schlinker and Amiet [32] has been obtained by fitting the experimental flat-plate wall pressure experimental data by Willmarth and Roos [35]. It reads

$$\begin{aligned} \frac{\phi_{pp}(\omega\delta^*/U_e)}{[(1/2)\rho U_e^2](\delta^*/U_e)} = {} & 2\times 10^{-5}\left[1 + \left(\frac{\omega\delta^*}{U_e}\right) + 0.217\left(\frac{\omega\delta^*}{U_e}\right)^2\right. \\ & \left. + 0.00562\left(\frac{\omega\delta^*}{U_e}\right)^4\right]^{-1} \end{aligned} \quad \text{(A5)}$$

To reproduce the wall pressure spectrum at the trailing edge of a NACA-0012 airfoil, Schlinker and Amiet [32] proposed the following empirical correction factor:

$$\chi = 10^{(2.29782 - 1.624180\varpi + 0.430079\varpi^2 + 0.678058\varpi^3 - 0.564063\varpi^4)/10} \quad \text{(A6)}$$

where $\varpi = \log(\omega\delta^*/U_e)$.

Acknowledgments

The jet-noise measurements have been carried out in the framework of the European Union (EU) 7th Framework Project ACP8-GA-2009-234313-OPENAIR (optimisation for low environmental noise impact aircraft). The NACA-0012 computational fluid dynamics simulations have been carried out in the framework of the EU 7th Framework Clean Sky Project JTI-CS-2009-1-GRA-02-004 ADOCHA (acoustic development of conventional high-lift architectures). The authors are particularly grateful to Thomas Castelain and Pascal Souchotte of École Centrale de Lyon, to Malcolm Smith of University of Southampton, and to Tilman Hetsch of the Aircraft Research Association.

References

[1] Ewert, R., "CAA Slat Noise Studies Applying Stochastic Sound Sources Based On Solenoidal Digital Filters," AIAA Paper 2005-2862, May 2005.

[2] Ewert, R., Appel, C., Dierke, J., and Herr, M., "RANS/CAA Based Prediction of NACA 0012 Broad-band Trailing Edge Noise and Experimental Validation," AIAA Paper 2009-3269, May 2009.

[3] Kraichnan, R. H., "Diffusion by a Random Velocity Field," *Physics of Fluids*, Vol. 13, No. 1, 1970, pp. 22–31. doi:10.1063/1.1692799

[4] Fung, J. C. H., Hunt, J. C. R., Malik, N. A., and Perkins, R. J., "Kinematic Simulation of Homogeneous Turbulence by Unsteady Random Fourier Modes," *Journal of Fluid Mechanics*, Vol. 236, 1992, pp. 281–318. doi:10.1017/S0022112092001423

[5] Careta, A., Sagues, F., and Sancho, J., "Stochastic Generation of Homogeneous Isotropic Turbulence with Well-Defined Spectra," *Physical Review E (Statistical Physics, Plasmas, Fluids, and Related Interdisciplinary Topics)*, Vol. 48, No. 3, 1993, pp. 2279–2287. doi:10.1103/PhysRevE.48.2279

[6] Béchara, W., Bailly, C., Lafon, P., and Candel, S., "Stochastic Approach to Noise Modeling for Free Turbulent Flows," *AIAA Journal*, Vol. 32, No. 3, 1994, pp. 455–464. doi:10.2514/3.12008

[7] Bailly, C., and Juvé, D., "A Stochastic Approach to Compute Subsonic Noise Using Linearized Euler's Equations," AIAA Paper 1999-1872, May 1999.

[8] Billson, M., Eriksson, L., and Davidson, L., "Jet Noise Modeling Using Synthetic Anisotropic Turbulence," AIAA Paper 2004-3028, 2004.

[9] Ewert, R., "Slat Noise Trend Prediction Using CAA with Stochastic Sound Sources from a Random Particle-Mesh Method (RPM)," AIAA Paper 2006-2667, 2006.

[10] Ewert, R., "Broadband Slat Noise Prediction Based on CAA and Stochastic Sound Sources from a Random Particle-Mesh (RPM) Method," *Computers and Fluids*, Vol. 37, No. 4, 2008, pp. 369–387.

[11] Dieste, M., and Gabard, G., "Random-Vortex-Particle Methods for Broadband Fan Interaction Noise," AIAA Paper 2010-3885, June 2010.

[12] Powell, A., "Theory of Vortex Sound," *Journal of the Acoustical Society of America*, Vol. 36, 1964, pp. 177–195. doi:10.1121/1.1918931

[13] Crow, S. C., "Aerodynamic Sound Emission as a Singular Perturbation Problem," *Studies in Applied Mathematics*, Vol. 49, 1970, pp. 21–44.

[14] Lighthill, M. J., "On Sound Generated Aerodynamically: 1. General Theory," *Proceedings of the Royal Society of London A*, Vol. A211, No. 1107, 1952, pp. 564–578. doi:10.1098/rspa.1952.0060

[15] Brooks, T., Pope, D., and Marcolini, M., "Airfoil Self-Noise and Prediction," NASA TR 1218, 1989.

[16] Amiet, R. K., "Noise Due to Turbulent Flow Past a Trailing Edge," *Journal of Sound and Vibration*, Vol. 47, No. 3, 1976, pp. 387–393. doi:10.1016/0022-460X(76)90948-2

[17] Howe, M. S., "Contributions to the Theory of Aerodynamic Sound, with Application to Excess Jet Noise and the Theory of the Flute," *Journal of Fluid Mechanics*, Vol. 71, 1975, pp. 625–673. doi:10.1017/S0022112075002777

[18] Amestoy, P. R., Duff, I. S., and Excellent, J. Y. L., "Multifrontal Parallel Distributed Symmetric and Unsymmetric Solvers," *Computational Methods in Applied Mechanics and Engineering*, Vol. 184, 2000, pp. 501–520. doi:10.1016/S0045-7825(99)00242-X

[19] Casalino, D., and Barbarino, M., "A Stochastic Method for Airfoil Self-Noise Computation in Frequency-Domain," AIAA Paper 2010-3884, June 2010.

[20] Pierce, A. D., "Wave Equation for Sound in Fluids with Unsteady Inhomogeneous Flow," *Journal of the Acoustical Society of America*, Vol. 87, No. 6, 1990, pp. 2292–2299. doi:10.1121/1.399073

[21] Casalino, D., "*Benchmarking of Different Wave Models for Sound Propagation in Non-Uniform Flows*," *Procedia Engineering*, Vol. 6, 2010, pp. 163–172. doi:10.1016/j.proeng.2010.09.018

[22] Casalino, D., and Jacob, M., "Prediction of Aerodynamic Sounds from Circular Rods via Spanwise Statistical Modeling," *Journal of Sound and Vibration*, Vol. 262, No. 4, 2003, pp. 815–844. doi:10.1016/S0022-460X(02)01136-7

[23] Andersson, N., Eriksson, L. E., and Davidson, L., "Large-Eddy Simulation of a Mach 0.75 Jet," AIAA Paper 2003-3312, May 2009.

[24] Simonich, J. C., Narayanan, S., Barber, T. J., and Nishimura, M., "Aeroacoustic Characterization, Noise Reduction, and Dimensional Scaling Effects of High Subsonic Jets," *AIAA Journal*, Vol. 39, No. 11, 2001, pp. 2062–2069. doi:10.2514/2.1228

[25] Thies, A., and Tam, C. K. W., "Computation of Turbulent Axisymmetric and Nonaxisymmetric Jet Flows Using the $K-\epsilon$ Model," *AIAA Journal*, Vol. 34, No. 2, 1996, pp. 309–316. doi:10.2514/3.13065

[26] Freund, J. B., "Noise Sources in a Low-Reynolds-Number Turbulent Jet at Mach 0.9," *Journal of Fluid Mechanics*, Vol. 438, 2001, pp. 277–305. doi:10.1017/S0022112001004414

[27] Bogey, C., and Bailly, C., "Computation of a High Reynolds Number Jet and its Radiated Noise Using Large Eddy Simulation Based on Explicit Filtering," *Computers and Fluids*, Vol. 35, 2006, pp. 1344–1358. doi:10.1016/j.compfluid.2005.04.008

[28] Fleury, V., Bailly, C., Jondeau, E., Michard, M., and Juvé, D., "Space-Time Correlations in Two Subsonic Jets Using Dual Particle Image Velocimetry Measurements," *AIAA Journal*, Vol. 46, No. 10, 2008, pp. 2498–2509. doi:10.2514/1.35561

[29] Pagano, A., Barbarino, M., Casalino, D., and Federico, L., "Tonal and Broadband Noise Calculations for Aeroacoustic Optimization of a Pusher Propeller," *Journal of Aircraft*, Vol. 47, No. 3, 2010, pp. 835–848. doi:10.2514/1.45315

[30] Roger, M., and Moreau, S., "Bach-Scattering Correction and Further Extensions of Amiet's Trailing Edge Noise Model, Part 1: Theory," *Journal of Sound and Vibration*, Vol. 286, No. 3, 2005, pp. 477–506. doi:10.1016/j.jsv.2004.10.054

[31] Moreau, S., and Roger, M., "Competing Broadband Noise Mechanisms in Low-Speed Axial Fans," *AIAA Journal*, Vol. 45, No. 1, 2007, pp. 48–57. doi:10.2514/1.14583

[32] Schlinker, R. H., and Amiet, R. K., "Helicopter Trailing Edge Noise," NASA CR-3470, 1981.

[33] Chase, D. M., "Modeling the Wavevector-Frequency Spectrum of Turbulent Boundary Layer Wall Pressure," *Journal of Sound and Vibration*, Vol. 70, No. 1, 1980, pp. 29–67. doi:10.1016/0022-460X(80)90553-2

[34] Goody, M., "Empirical Spectral Model of Surface Pressure Fluctuations," *AIAA Journal*, Vol. 42, No. 9, 2004, pp. 1788–1794. doi:10.2514/1.9433

[35] Willmarth, W. W., and Roos, F., "Resolution and Structure of the Wall Pressure Field Beneath a Turbulent Boundary Layer," *Journal of Fluid Mechanics*, Vol. 22, 1965, pp. 81–94. doi:10.1017/S0022112065000599

C. Bailly
Associate Editor